Trabajo de Fin de Máster

SEARCHING FOR COMPACT GALAXIES IN MaNGA

Autoría

Pau Grèbol Tomàs

Tutorizado por

Dra. Anna Ferré-Mateu (IAC)
Dra. Helena Domínguez-Sánchez (CEFCA)

Máster Universitario en Astrofísica

- Enero de 2023 -

Resumen

Objetivos: Presentamos el análisis de la muestra de MaNGA DR17 para caracterizar su población de galaxias compactas. Nos centramos en aquellas que permitan rellenar el rango en masa entre galaxias elípticas compactas ($8 \lesssim \log(M_\star/M_\odot) \lesssim 10$) y galaxias masivas compactas ($10 \lesssim \log(M_\star/M_\odot)$). Estudiamos sus poblaciones estelares y cinemática para relacionar las galaxias compactas a diferentes rangos de masa. Además, se pretende discutir cómo han sido los procesos de formación de las galaxias estudiadas.

Metodología: Utilizamos los catálogos PyMorph y Deep Learning de MaNGA para obtener los valores de radio, masa y clasificación morfológica necesarios para el análisis. Con ellos se clasifican las galaxias según su morfología y luego se selecciona un total de 37 galaxias compactas, de acuerdo con su masa estelar y su radio efectivo (R_e). Usando la técnica del *full spectral fitting* derivamos sus poblaciones estelares y sus historias de formación estelar a partir del conjunto de los espectros apilados en 1 R_e. Seguidamente, se aplica un algoritmo para agrupar las galaxias es tres grupos según sus propiedades. De forma preliminar se ha utilizado la tecnología IFU de MaNGA para construir los mapas de las propiedades estudiadas. A partir de ellos se han construido los respectivos perfiles radiales.

Resultados: Se han comparado las propiedades de las galaxias seleccionadas con las de otras galaxias compactas a diferentes rangos de masa. Con ello identificamos un grupo que muestra propiedades similares a las galaxias masivas reliquia, i.e. galaxias que no han sufrido ninguna interacción desde su formación inicial en $z \sim 2$. Otro grupo muestra una formación estelar extendida en el tiempo, que es propia de canales de formación intrínsecos. Finalmente, el tercer grupo presenta historia de formación estelar picuda inicialmente. Después de un tiempo inactiva, se retomó para formar la masa restante. Se especula que puede ser a causa de procesos de interacción con otras galaxias.

Conclusiones: Las galaxias seleccionadas ocupan satisfactoriamente rango de masas entre las galaxias elípticas compactas y las galaxias masivas compactas. Las propiedades de nuestras galaxias son compatibles con la suposición que las relaciones de escala de las galaxias compactas difieren de las que muestran las galaxias extendidas. Con ello, se confirma que las galaxias compactas a diferentes masas están relacionadas. Finalmente, se ha vinculado cada grupo con un camino de formación diferente. En futuros trabajos con tecnología IFU se prevé confirmar el camino de formación que ha seguido cada galaxia individual.

Contents

1 Introduction and objectives

Our current understanding of the Universe is based on a Λ-CDM (initials for *cold dark matter*) cosmology in which dark matter particles clump to form large structures in the early Universe. These are the dark-matter halos, which embed baryonic mass [1]. Baryonic mass, although being the least abundant in the Universe, is one of the main shapers for galaxy formation and evolution. The best estimate of the number of galaxies in the Universe is over $3 \cdot 10^{12}$ galaxies [2]. Therefore, galaxies are one of the main building blocks of the Universe and it is crucial to understand how they form and evolve to draw conclusions at larger scales.

Given the vast number of galaxies, they all show different characteristics. This is why galaxies are usually grouped by properties. They can be passive, star-forming, dwarf, massive... Every galaxy can help to shed light when trying to unveil the origin of the Universe and its evolution. With this idea, this Master Thesis aims to study a particular group of galaxies, the so-called compact galaxies.

1.1 Galaxy analysis and properties

1.1.1 Morphology: ETGs and LTGs

One of the main ways of classifying galaxies is related to their morphology, how they look like. The original morphological classification for galaxies is the Hubble sequence [3] (Figure 1.1). In general terms, we distinguish late-type galaxies (LTGs), which are mainly identified for featuring spiral arms, as well as a central bulge. LTGs can also present a central bar. On the other hand, early-type galaxies (ETGs) do not present visible features, excepting a central bulge.

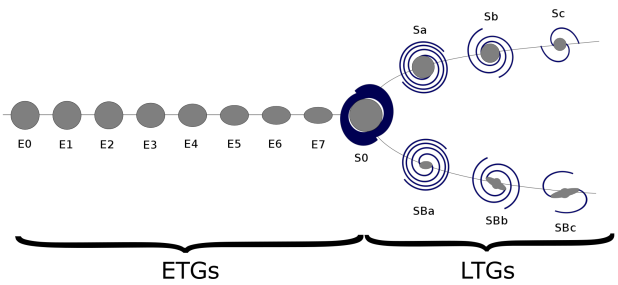

Figure 1.1: Scheme of the Hubble Tuning Fork Diagram [3]. Galaxies are mainly classified between early-type galaxies (ETGs) and late-type galaxies (LTGs) based on their morphology. Modified image from Wikimedia.

Even though this is purely a 'visual' morphological classification, ETGs and LTGs show clear differences in terms of their stellar populations. ETGs usually feature old stars and low star formation rates. These are old objects that appear red, photometrically, and have been considered in most cases

to be 'dead', i.e. have ceased their star formation. On the contrary, LTGs are blue, gas-rich objects, which continuously form stars.

Kinematically, ETGs and LTGs also show general differences in the way their stars move within the galaxy. Two main parameters to characterize these properties are the rotational velocity, v, and the velocity dispersion, σ (Section 3.1.1). In a pressure supported system, stars do not have a preferred moving direction. This is the case of ETGs, which typically show high σ values. A system is rotationally-supported if their stars move in a determined direction, which is the case of LTGs [4–7]. These objects are dominated by rotation and thus show large v/σ ratios.

1.1.2 Photometry

The Hubble sequence was one of the first ways to classify galaxies. It was a pure morphological classification. However, it relied on visual analysis and had several drawbacks, mainly subjectivity. Current galaxy classifications are based on photometric decomposition, analyzing light distributions from different regions of the galaxy. This allows to identify the galaxy elements (e.g. bulge, disk, bar) by fitting the luminosity profile to pre-defined parametric models. The total luminosity distribution of a galaxy is expected to be the sum of the luminosity distributions of its components.

One could define that a galaxy ends where no more light is seen. However, this definition is tricky, because it depends on the sensibility of the detectors and also on the filter used. The effective radius, R_e, is a useful magnitude to characterize the size of a galaxy. It is defined as the radius embedding half of the total light emitted by the galaxy. But this value depends on the light distribution. If a galaxy has a concentrated amount of stars in the central region, i.e. in a bulge, it will have a smaller effective radius than a more diffuse galaxy of the same physical size.

Light profiles are built by measuring the flux as a function of radius. The light from a given point is the sum of all the contributions along the line of sight. This is why it is common to mathematically describe the light profiles for the different galaxy elements. The most used one for describing galaxy bulges and disks is the Sérsic profile [8], which is a monotonically decreasing function, having its maximum intensity at the galaxy center. At a given radius r, the Sérsic profile is described as:

$$I(r) = I_e \cdot e^{-b_n\left[\left(\frac{r}{R_e}\right)^{1/n}-1\right]} \tag{1.1}$$

where n is the so-called Sérsic index, $b_n = 2n - 0.327$ is a parametric function, R_e is the effective radius and I_e is the element intensity at R_e. If light profiles are expressed as one component, Sérsic is commonly used. Typically, disks are well described with a Sérsic profile with $n = 1$ and bulges with $n \sim 4$.

On the other hand, the galaxy disk luminosity can also be well-described by an exponential profile [9]:

$$I_d(r_d) = I_{0,d} \cdot e^{-r_d/h} \tag{1.2}$$

where $I_{0,d}$ is the disk contribution at the center of the galaxy and h is a scale parameter. It is common to describe galaxy light profiles as one component (Sérsic profile) or two component (a disk plus a bulge), known as Sérsic+Exponential profile. There are other mathematical functions used to describe the luminosity profile of a galaxy (e.g. Ferrers profile [10] for bars).

1.1.3 Stellar populations

The overall properties of galaxies that are not located in our neighborhood are mostly described by the integrated properties of the stars conforming the galaxy. The current stellar evolution paradigm states that the most massive stars are those with shortest lifetimes, but also the most luminous, specially in the blue bands. On the contrary, less massive stars are often the oldest ones, and they are indeed the faintest, emitting most of their light at redder wavelengths. Thus, the measure of the fraction of low mass (red) stars is an indication of the age of the stellar population. The distribution of the number of stars at a given mass m that are produced in a star burst is given by the initial mass function (IMF, [11]). This is expressed as a power law:

$$\log\left(\phi(m)\right) = \Gamma \cdot \log m + C. \tag{1.3}$$

The most important parameter of this distribution is the IMF slope, Γ. It characterizes the amount of low-mass stars that were created in a star-forming burst.

One of the most relevant parameters related to the chemical composition of galaxies is metallicity. It represents the abundance of a certain chemical element X, heavier than hydrogen and helium. The metallicity is calculated from the measured abundance of a given X element compared with that of the Sun, e.g:

$$[X/H] = \log\left(\frac{N_{\mathrm{X}}}{N_{\mathrm{H}}}\right)_{\star} - \log\left(\frac{N_{\mathrm{X}}}{N_{\mathrm{H}}}\right)_{\odot}. \tag{1.4}$$

For galaxies, the most commonly used metallicity parameters are the total stellar metallicity, [Z/H], and its iron abundance, [Fe/H] [12–14]. The total stellar metallicity accounts for the overall metallic elements fraction.

Another crucial parameter to understand the formation and evolution of a galaxy is related to the abundance of the α-elements [15–18]. These are those byproducts of helium burning reactions, such as carbon, oxygen, magnesium or neon. Produced in the early stages of the stellar evolution, α-elements are mostly released by supernova explosions. Delayed in time, heavier stars explode as Type Ia supernovae, releasing iron to the interstellar medium. The newborn stars would be enriched by those elements in the interstellar medium. The [α/Fe] ratio is often used as a 'clock' to establish how fast the galaxy formed its stars. A high [α/Fe] value can represent a fast formation process, while a low [α/Fe] value would represent a slow star-forming process [19–21].

1.2 The Realm of compact galaxies

As mentioned above, galaxies come in different shapes and masses. The current mass-size relation in the local Universe shows that more massive galaxies tend to be bigger than less massive ones, e.g.

[22, 23]. Another way to classify them is by their compactness. This is a property that describes the density of a galaxy, with compact galaxies having their stellar mass confined in small radii. In fact, it is well established that massive galaxies were much more compact in the early Universe at a given mass, e.g. [24–26], than those we see nowadays. This is understood as a strong evolution in the size of the overall population, given by the formation processes these galaxies follow [27]. Nonetheless, compact galaxies are also found in the local Universe, covering approximately 5 orders of magnitude in stellar mass. These galaxies are outliers of the mass-size trend described by usual extended galaxies, and are all ETG-like.

Compact galaxies can be characterized according to their stellar mass, as seen in Figure 1.2. At the lowest stellar masses, $\log(M_\star/M_\odot) \lesssim 8$, ultra compact dwarf galaxies (UCDs) present the smallest projected effective radii (up to $R_e \lesssim 100$ pc), making them the most compact galaxies in the Universe, e.g. [28–30]. In the intermediate mass range ($8 \lesssim \log(M_\star/M_\odot) \lesssim 10$), compact elliptical galaxies (cEs) have sizes of $100 \lesssim R_e$ [pc] $\lesssim 900$, e.g. [31–33]. Finally, the massive end of the compact galaxy realm is populated by compact massive galaxies (CMGs), with $\log(M_\star/M_\odot) > 10$ and $\mathrm{R}_e < 1.5$ kpc [34]. The latest studies of compact galaxies at different mass ranges have suggested that their properties can be scaled in terms of stellar mass, e.g. [35]. Under these hypotheses, UCDs would be low-mass analogues for compact ellipticals, with their size, metallicity and luminosity transformed accordingly. This is reinforced by the already-seen trends in kinematics and stellar populations between compact galaxies at wider mass ranges.

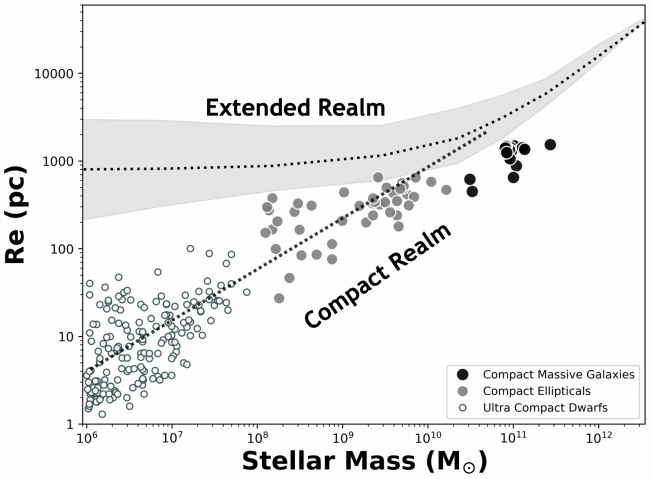

Figure 1.2: General scheme of the current stellar mass-size plane. Compact galaxies are outliers of the local distribution and are also classified by mass. CREDITS: ANNA FERRÉ-MATEU.

1.2.1 Compact galaxy formation

The current galaxy formation paradigm states that galaxies grow in a two-phase formation scenario [36–40]. In the first phase, which takes place at the earliest phases of the Universe, a gas-rich star-forming system is created [41]. The result is an extremely compact object, often referred to as a *blue nugget*. These galaxies show blue colors and high luminosity [42], fuelled by an intense star formation (SFR$\geq 10^3 \mathrm{M}_\odot$ yr^{-1}; [43]). At some stage this dissipative phase ends, and the compact object quenches, becoming a massive, red and metal-rich object. As shown in the top left formation channel of Figure 1.3, these CMGs, also nick-named *red nuggets* [44–47], mark the end of the first phase of formation, by $z \sim 2$. The second phase of ETGs formation is driven by dry minor merger events, inducing the growth of the red nugget by adding accreted material in the outskirts of the galaxies. This process can explain the mild grow over cosmic time in stellar mass but the large increase in size, ending up being the massive ETGs we observe at $z = 0$ [24, 26, 48].

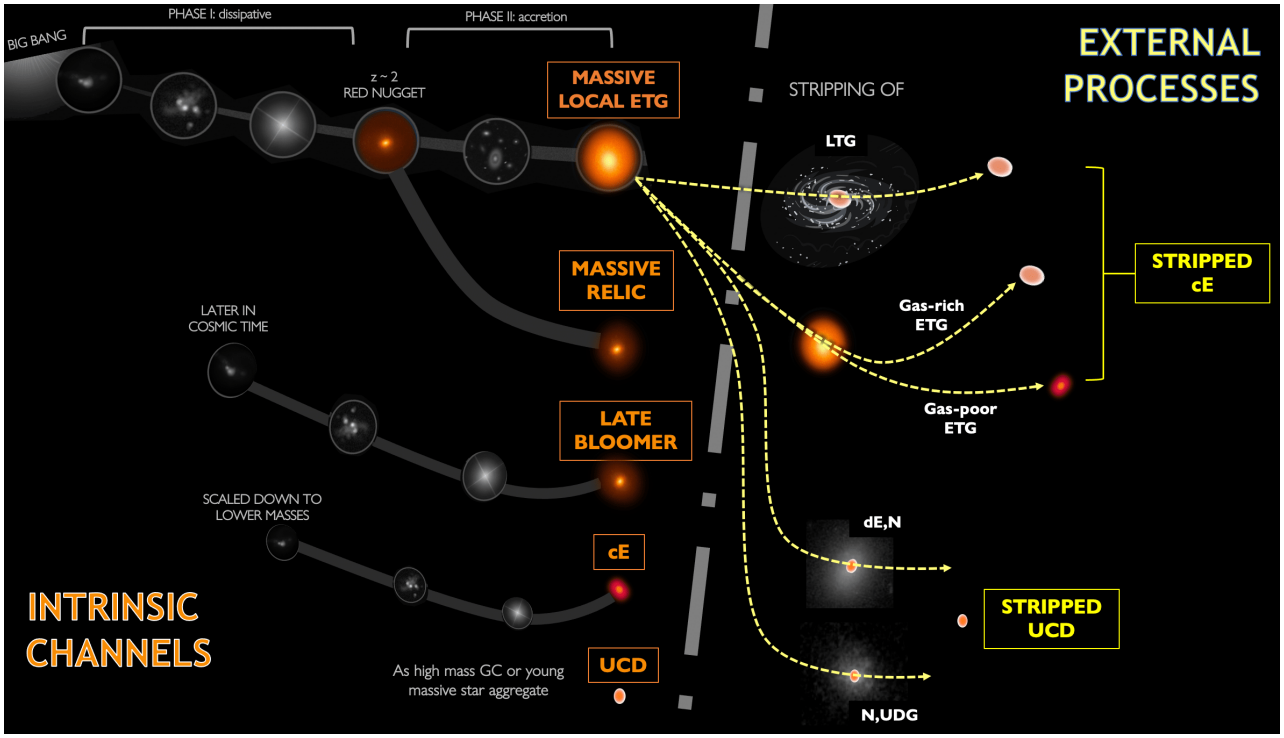

Figure 1.3: Scheme showing the different formation pathways that can be followed by a compact galaxy in the local Universe. The current paradigm agrees on a common initial formation phase, depicted in the top-left corner. Once the red nugget is born, the compact galaxy can follow either in-situ processes (left) or ex-situ (right). Orange labels depict objects that are the result of intrinsic processes. Yellow labels stand for objects that are the result of stripping processes. Note that the galaxy resulting from a stripping depends on the progenitor type. CREDITS: ANNA FERRÉ-MATEU.

Compact massive galaxy formation channels

Because the second phase is driven by stochastic events, there is the extremely rare probability that a galaxy avoids such interactions. In this case, it will remain unchanged since the red nugget phase, thus presenting the properties of this early stage [44, 49, 50]. These untouched galaxies, found at $z \sim 0$, are therefore nick-named *relic galaxies*. They are crucial to study the early Universe, but with the ease of a spectral and spatial resolution of galaxies in the local Universe. Theoretical models predicting red nuggets survival are sensitive to galaxy merging processes [51], expecting that 0.15% of the massive galaxies formed at $z \simeq 2$ could end up being a massive relic galaxy [52].

The current number of confirmed massive relic galaxies up to z∼0.5 is 13 [53–55]. These massive relic galaxies all feature a high stellar mass ($\log(M_\star/M_\odot) > 11$) and small radius ($R_e < 1$ kpc), with a fast star formation episode as early as at the time of the Big Bang ($t \sim t_{BB} \sim 14$ Gyr). They all present disky morphologies, similar to those in observed massive red nuggets [25, 53, 56]. But not all massive compact galaxies are relics of the early Universe. Numerous other CMGs found in the local Universe, despite sharing similar structural properties to the relic counterparts, present stellar populations with extremely young ages and slightly lower metallicites (e.g. [44, 57–60]). How these galaxies are formed still poses a great enigma. One possibility is that they are galaxies that are now undergoing the first-phase, delayed red nuggets in the making, or 'late bloomers' [35, middle evolutionary channel in Figure 11]. It could also be possible that some of these younger CMGs were the remnants of a more massive galaxy that lost its stars due to external processes, such as stripping. However, this seems a

more unlikely formation channel, as many of the seen properties do not support it. Overall, CMGs are thought to be formed by in-situ processes rather than external ones.

CMGs are found in all environments, although they seem to thrive in clusters of galaxies [23, 50, 61–63]. This is a combination of serendipitousness (e.g. finding them in a cluster is easier, as clusters are interesting systems by themselves and are frequently observed with different facilities), but also due to the extreme conditions of the cluster itself. The high gravitational fields accelerate the galaxies, and given their high velocities, this prevents mergers from taking place, promoting the occurrence of massive relic galaxies. Conditions in the field are expected to happen slightly later and with milder conditions, therefore galaxies in this environment will tend to be less extreme in their properties. A 'degree of relicness' linked to the environment was proposed in Ferré-Mateu *et al.* [54] and it was later confirmed with the *INvestigating Stellar Population In RElics* (INSPIRE) survey, the largest sample of massive relics to date [64].

Low mass compact galaxy formation channels

As we move towards intermediate and lower stellar masses, the leading formation mechanism changes from an in-situ based to external processes playing a more relevant role. In fact, this change seems to occur around the characteristic mass scale of $3\times10^{10}M_{\odot}$, e.g. [35, 65], where several relations of ETGs seem to experience relevant changes in their nature.

Compact elliptical galaxies, cEs, are usually thought to be the remnant of stripping a dwarf elliptical or a low-mass galaxy (either ETG or spiral; e.g. [31, 32, 66–68]). However, some of these galaxies are also expected to form in-situ, defining cEs like the true low-mass end of ETGs, e.g. [69–72]. As a result, cEs are thought to be a mix-bag of objects, with different evolutionary channels (see the bottom and right side of Figure 1.3 for cEs formation channels). In the case where the cE have an external origin, this is further supported by the large SMBHs typically found in their centers, e.g. [35, 68, 73, 74]. However, the strongest evidence for this evolutionary path is that some cEs have been found being currently stripped by a larger, nearby galaxy, e.g. [75–77]. cEs formed this way are thus expected to be outliers in most of their scaling relations, such as with its black hole or for the mass-metallicity relation, e.g. [35, 72, 78–80]. Nonetheless, evidence for some cEs being formed in-situ has also been found, mostly outside the cluster environment, where stripping is not as likely to happen [71, 72, 77, 80–82]. For cEs formed following this in-situ formation, it is expected that they will follow the expected scaling relations as the true low-mass end of ETGs.

Similarly, as in cEs, UCDs are assumed to be the result of the stripping of a larger galaxy. The stripping results in the bare core of an original dwarf galaxy [33, 83–85], showing the stellar populations properties of the original host galaxy. On the other hand, an UCD could also be star cluster aggregates, or simply the high-mass end of globular clusters [86–88]. This last type of UCD would be the most similar to the true low-mass end of the compact realm, but it is not expected that many follow this in-situ process.

Unfortunately, we do not yet have a complete census for compact galaxies and their preferred origin (in-situ vs. ex-situ). This is mainly due to the incomplete samples we have at hand, as the realm of

compact galaxies has been developed only during the last ∼20 years. However, Ferré-Mateu *et al.* [35] suggested that there may be a connection between these families, in particular between cEs and CMGs. In their mass-size relation plot [35, Figure 11], they noticed that the distribution of CMGs and cEs presented similar stellar populations with continuity, but also share similar kinematic features. It was thus suggested that cEs could also be either the stripped result of a CMG or that they also formed as the low-mass tail of the CMG distribution. In this case, one could also find an intermediate-mass relic, a downsized version of a massive relic galaxy. Interestingly, there was a noticeable gap in stellar mass between these two groups of compact galaxies (cEs and CMGs), which could be the clue to reveal whether such connection exist in reality.

To this end, the following study is aimed at looking for galaxies that bridge this mass-size gap. We search for compact galaxy candidates in the MaNGA survey to study their kinematic and stellar populations properties. We study their global, integrated values but also in a spatially-resolved way to study their 2D maps and profiles. With this, we can better elucidate their origin and plausible relation of galaxies in the mass gap, while we particularly aim at finding possible relic galaxies in this sample.

2 Sample selection

In this chapter we present the data used to search for compact galaxies in the local Universe. The chosen survey has several value added catalogs (VACs), which provide different parameters for its galaxies. We also describe in this chapter the VACs used in this project and how the data is analysed. Based on the properties of compact galaxies found in literature, we define a new criterion to select them and apply it to our sample.

2.1 MaNGA survey and Value Added Catalogs

Mapping Nearby Galaxies at APO (MaNGA) [89] is a *Sloan Digital Sky Survey* (SDSS) [90] survey. With its latest data release, DR17, it has obtained spatially resolved information of over 10000 galaxies at $z < 0.17$. This survey takes advantage of the *Integrated Field Unit* (IFU) technology to acquire spatially resolved spectroscopy. Each galaxy from the survey is dissected over the fibers at each IFU. Spectroscopic data is obtained from the BOSS spectrograph [91, 92], at the Sloan Telescope [93, 94]. Each galaxy data is presented as a *datacube*, where two dimensions encode the 2D spatial information and the third dimension expresses the results from the BOSS spectroscopy. Each object in the survey is uniquely tagged by a *Plate-IFU* number. The reader is referred to Bundy *et al.* [89] for a more extensive description of the survey.

A MaNGA VAC is a catalog which contains relevant and complementary properties for the MaNGA sample. There are several MaNGA VACs available. We now present those that are useful for our study:

- MaNGA PyMorph catalog [95]: provides parameters from fitted Sérsic and Sérsic+Exponential profiles to the 2D surface brightness profiles of MaNGA DR17 galaxies. From these we use the effective radii, axis ratios and galaxy luminosities. The latter are translated into a stellar mass using the mass-to-light ratios from Mendel *et al.* [96]. The MaNGA PyMorph catalogue provides a flagging system (`FLAG_FIT`) which separates galaxies that are better described by a Sérsic or a Sérsic+Exponential profile. We thus use the parameters returned by the optimal model for each galaxy. When `FLAG_FIT` $= 0$ (both models are acceptable), we use the parameters returned by the Sérsic+Exponential parametrization.

- MaNGA Deep Learning Morphological Value Added catalog (MDLM-VAC) [97]: provides morphological information based on supervised deep learning algorithms using Convolutional Neural

Networks. It includes a series of binary classifications which separate early from late type galaxies (ETGs vs. LTGs), pure ellipticals (Es) from lenticulars (S0), barred from non-barred galaxies and edge-on from non-edge on galaxies. In addition, the catalog also reports a T-Type value, analogue to the Hubble sequence [3].

- MaNGA Firefly value-added catalog [98, 99]: provides measurements of spatially resolved stellar population properties in MaNGA galaxies. It involves stellar population model fitting using the FIREFLY full spectral fitting code [100] with MILES-11 and MaStar stellar population models [101, 102]. A spatial Voronoi binning [103] is applied to achieve a signal-to-noise (S/N) bin value of 10. This enhances the spectral information trustworthiness, but it loses spatial information.

2.2 MaNGA compact galaxy sample selection

First, we use the MDLM-VAC to make an initial classification of the MaNGA galaxies. This is based on the morphology, as compact galaxies are expected to be ETGs. We thus select galaxies with and ETG morphology: `T-Type<0` and `PS0<0.5`. The selection results in 3834 out of 10293 galaxies from the MaNGA DR17 parent sample.

We then select compact galaxies by imposing a given mass and size criteria. There is a vast number of criteria in the literature used to define compact galaxies, particularly for CMGs, e.g. [60, 104, 105]. Because here we are aiming to fill the gap that covers the high-mass end of cEs with the low-mass end of CMGs, we impose the following limits:

- $M_\star > 10^9\ M_\odot$
- $R_e < 2$ kpc
- $\log(\Sigma_{1.5}) > 10.3$ dex

being $\Sigma_{1.5} = \frac{M\ [M_\odot]}{(R_e\ [\mathrm{kpc}])^{1.5}}$ a modified surface mass density, as in Barro *et al.* [106]. The first condition is set to select all galaxies with stellar masses that cover the high-mass end of cEs, targeting the gap in stellar mass [see e.g. 35, Figure 11]. The second corresponds to the largest size limit used to select compact galaxies at the high-mass end [60, 107]. And the third assures the compactness of the candidate (based on [106–108]).

We show in Figure 2.1 the stellar mass-size plane for the complete sample of 10293 MaNGA DR17 galaxies. The black dash-dotted line expresses the compactness limit used in this work, as described by the condition based on $\Sigma_{1.5}$ above. The upper R_e limit is shown as a horizontal dashed black line. Circles represent ETGs according to the MaNGA Deep Learning catalog, while crosses show S0 galaxies and LTG. All galaxies falling below the intersection of the used criteria are considered compact galaxies for this work. A total of 38 compact galaxies are thus selected, being all of them ETGs. After a visual inspection, we discard object 8092-12794 as it corresponds to two interacting galaxies. Our final sample thus consists of 37 compact galaxies. The stellar masses, radii and redshifts[1] are specified in Table 2.1.

[1] From the NASA-Sloan Atlas catalog: `https://www.sdss4.org/dr17/manga/manga-target-selection/nsa/`

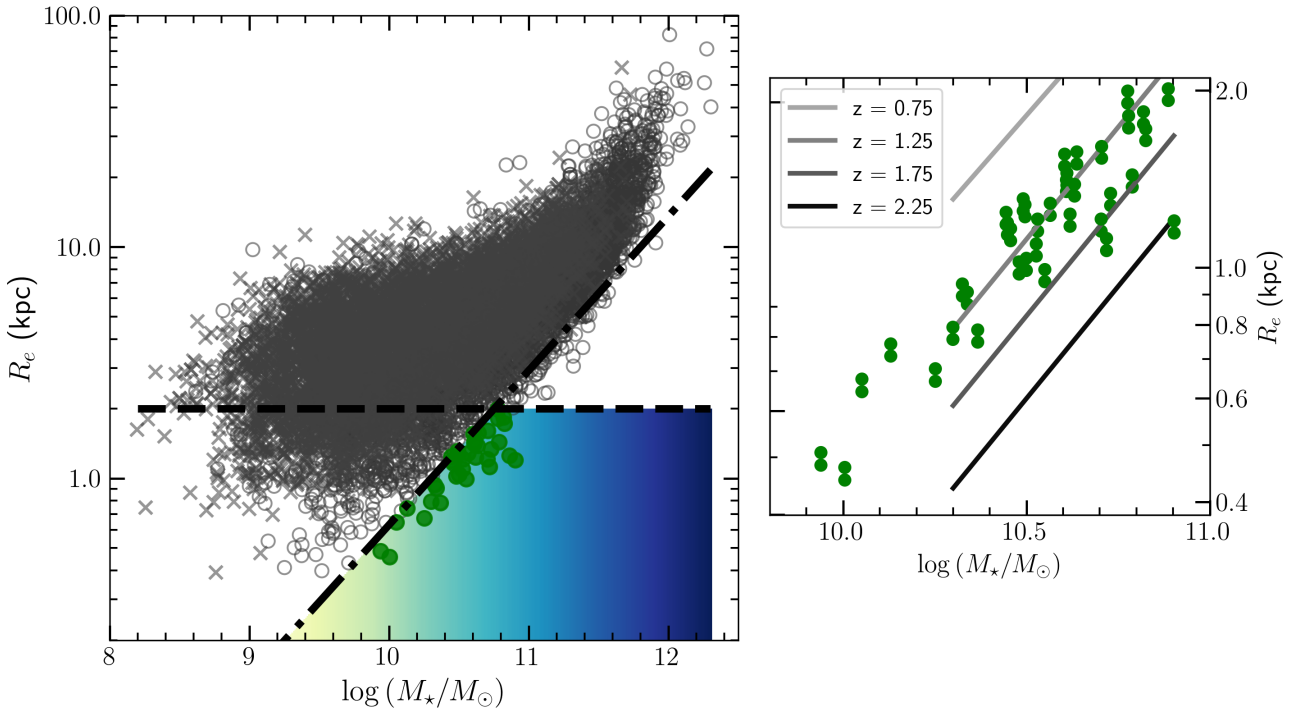

Figure 2.1: Stellar mass vs. effective radius. *Left:* for the full MaNGA DR17 dataset (10293 nearby galaxies). Crosses indicate spiral or $S0$ galaxies, while circles represent elliptical galaxies. The dash-dotted black line represents the compactness criterion defined in Section 2.2. The black dashed line marks the upper threshold of $R_e = 2$ kpc. The background colors are used to help guide the eye over the different compact galaxies in terms of stellar mass. Yellowish colors represent the high-mass end of the cEs family, whereas the blue region represents the CMG region. All galaxies below the intersection of both lines are those that conform our sample of compact galaxies (green points), laying in the gap region colored by green-turquoise colors. *Right:* Different mass-size relations for ETG at various redshifts from van der Wel *et al.* [109] are plotted in a grayscale, along with the final 37 selected compact galaxies analyzed in this work. Our sample is mostly compatible with a redshift $z \sim 1.5$ mass-size relation.

The region corresponding to where compact galaxies would be located is colored in Figure 2.1. The yellowish region in Figure 2.1 shows the high-mass end of cEs, while CMGs are expected to be lay in the bluish parts. The galaxies selected for this work fall in the gap region, the green-turquoise zone. These mass limits are purely illustrative, as there is not a unique mass threshold in the literature to distinguish compact families.

According to the two-phase formation paradigm, compact galaxies should be already formed by at least $z \sim 2$, when the red nugget was formed. If compact galaxies in the gap are somehow the remnants of this early stage or directly connected to it, they should roughly match the mass-size relation at $z \sim 2$. For example, all massive relic galaxies studied to date are consistent with the mass-relation of $z \sim 2$ galaxies, e.g. [54, 55, 110]). In the right panel of Figure 2.1 we compare the final 37 selected compact galaxies to several mass-size relations at different redshifts (from van der Wel *et al.* [109] using CANDELS/3D-HST). We find that, although all the galaxies in our sample are found in the nearby Universe, they are in reality more compatible with the mass-size relations at $z \sim 1.25 - 1.75$. Only the most massive galaxy, 11020-1902, is compatible with a $z \sim$2 relation, making it the best candidate for a relic galaxy. We will discuss this particular galaxy in more detail later on.

Table 2.1: The 37 selected compact galaxies in the MaNGA survey. Each galaxy is labelled according to its Plate-IFU. Mass and radius values are obtained from the PyMorph VAC [95]. The redshift value is obtained from the NASA-Sloan Atlas catalog.

Plate-IFU	$\log(M_\star/M_\odot)$	R_e **(kpc)**	z
8443-1901	10.61	1.41	0.0294
8721-1901	10.55	0.99	0.0456
8323-1901	10.61	1.45	0.0253
9492-1901	10.46	1.16	0.0457
9042-1901	10.78	1.81	0.0729
7977-1901	10.05	0.65	0.0260
9869-1901	10.82	1.84	0.0309
8601-1902	10.44	1.24	0.0280
9507-1902	10.82	1.72	0.0517
8243-1902	10.53	1.21	0.0427
8616-1902	10.78	1.99	0.0302
8486-1902	10.34	0.91	0.0195
8464-3703	10.30	0.79	0.0398
8137-3703	10.49	1.31	0.0317
10216-3703	10.63	1.39	0.0466
10510-1901	10.00	0.46	0.0197
11011-1901	10.49	1.28	0.0270
11020-1902	10.90	1.20	0.0253
11827-1901	10.73	1.34	0.0265
11943-9102	10.50	1.04	0.0284
11945-1901	10.72	1.12	0.0292
11979-1902	10.70	1.61	0.0469
11984-1902	10.37	0.78	0.0464
8248-3704	10.70	1.21	0.0255
8710-1902	9.94	0.48	0.0214
9496-1902	10.48	1.02	0.0452
9880-1902	10.13	0.74	0.0255
11954-1902	10.45	1.19	0.0266
12067-3701	10.25	0.67	0.0379
7981-1902	10.79	1.44	0.0300
11015-1902	10.56	1.29	0.0241
11960-1902	10.89	2.01	0.0514
11967-3702	10.62	1.23	0.0458
11968-1902	10.60	1.56	0.0451
11969-1902	10.64	1.57	0.0493
12624-3702	10.32	0.94	0.0272
12673-1901	10.53	1.10	0.0274

3 Methodology

In this work we aim at characterizing the properties of compact galaxies bridging the gap between cEs and CMGs in the mass-size relation. In a first analysis (Section 5.1), we focus on their global properties, which allow us to compare them with other galaxies in the literature. We use a `.dpuser` code applied to the QFitsView tool [111] to obtain a stacked spectrum from the 2D datacubes of MaNGA. For each galaxy, we retrieve a single spectrum from the stacking of pixels within $1R_e$.

We also benefit from the IFU observations, which provide a spectrum for each spaxel of the datacube. This allows us to retrieve the properties of the galaxy in a spatially-resolved way (Section 5.2). The following sections describe the spectroscopic analysis, applied to both stacked and spaxel spectra.

3.1 Full spectral fitting

Most information of a galaxy regarding its stellar populations can be retrieved from its spectra. We take benefit from computational tools to estimate galaxy properties. Spectral fitting expresses a given spectrum and its properties as the weighted sum of model spectra. Each model spectrum is assumed to be representative of that of a star with given properties (e.g. mass, metallicity, age). From a full spectral fitting approach one can obtain some of the most relevant properties of a galaxy, such as the stellar kinematics (e.g. velocity dispersion), and its stellar populations (star formation histories, ages and metallicities).

Here we have obtained the kinematic and stellar populations using the Penalized Pixel-Fitting code (pPXF , [112]), implemented in the pPXF Python package [113], and the GandALF routine [114]. We used the full MILES stellar population models [115, 116] with a nominal spectral resolution of FWHM = 2.5 Å. The models cover stellar ages from 0.03 to 14 Gyr and metallicities between -2.27 and +0.40 dex. We considered the Base-models and a Kroupa-bimodal IMF with slope $\Gamma = 1.30$. Although massive relic galaxies have been shown to have steeper IMFs [54, 117] we have worked with a universal IMF to be able to compare with already published values. A more detailed analysis of this parameter will be carried in the future.

In the pPXF algorithm, the observed spectrum $G(x)$ is described as

$$G(x) = \sum_{k=1}^{K} w_k \left[B * T_k\right](x) + \sum_{l=0}^{L} b_l \mathcal{P}_l(x) \tag{3.1}$$

where T_k is the k-th spectrum of the T library, with K spectra. The broadening function is related to the line-of-sight velocity distribution (LOSVD) as $B(x) = \mathcal{L}(cx)$, being c the speed of light. $\mathcal{P}_l$ are the Legendre polynomials of order l and help to correct subtle differences between the templates and the actual spectrum. Overall, the pPXF algorithm finds the optimal weights (w_k and b_l) to fit the spectrum. As a final remark, pPXF can perform a regularization of templates weights, which smooths the resulting temporal distribution. However, in this work we have not applied any regularization method.

3.1.1 Stellar kinematics

Galaxy kinematics studies the movement of stars and gas within the galaxy. Once the galaxy spectra are corrected by its redshift, the velocity of the gas emitting a line is calculated using the Doppler effect formula. If we assume an emission line to have a gaussian shape, they can be parametrized by its central velocity, v_0, and the velocity dispersion, σ (Figure 3.1 and Equation 3.2).

$$I(v) = \frac{1}{\sqrt{2\pi\sigma^2}} e^{-(v-v_0)^2/2\sigma^2} \tag{3.2}$$

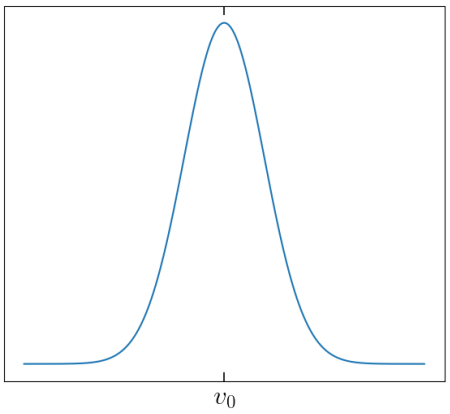

Figure 3.1: Gaussian distribution assumption for a velocity peak. The peak is characterized by the rotational velocity, v_0, and the velocity dispersion, σ, giving the width of the peak.

Since the gaussian shape is mainly described by v_0 and σ, these are also called the first and second order kinematic moments, respectively. The skewness of the distribution is the third momentum, denoted as h_3, and accounts for the asymmetry of the peak. The fourth momentum is the kurtosis, h_4, describing the sharpness of the peak. It kinematically represents the anisotropy of the movement[1].

For this analysis we used the pPXF routine with an additive Legendre polynomial of degree 5. This is used to correct the template continuum shape. It has been empirically proven that it is the correction that best optimizes the fitting errors. From this first pPXF iteration, we derive the recessional velocity and the galaxy velocity dispersion.

Another relevant kinematic parameter is the specific angular momentum, λ_R [118]. It provides information about the internal dynamics of the galaxy and it is commonly used to classify galaxies as fast or slow rotators, e.g. [119–121]. This dichotomy has been found to be related with the galaxy morphology, with most massive ETGs being more likely slow rotators [122]. Here we calculate the λ_R values as in Fischer, Domínguez Sánchez, and Bernardi [95], using the IFU observations provided by the MaNGA

[1]Formally, the LOSVD is expressed as a Gauss-Hermite series: $\mathcal{L}(v) = \frac{e^{-y^2/2}}{\sqrt{2\pi\sigma^2}}\left[1 + \sum_{m=3}^{M} h_m H_m(y)\right]$, where $y = (v - v_0)/\sigma$, H_m are the Hermite polynomials and the m momenta of the distribution include v_0, σ, h_3 and h_4[112].

survey. The λ_R is calculated as a weighted mean over the values in each spaxel:

$$\lambda_R = \frac{\sum_i^N R_i F_i \, |v_i|}{\sum_i^N R_i F_i \sqrt{v_i^2 + \sigma_i^2}}, \tag{3.3}$$

where R, F, v and σ denote the radial position, flux, rotational velocity and velocity dispersion at the i-th spaxel. The λ_R values are shown in Table 3.1. We were not able to estimate λ_R for those galaxies where there are no spaxels with $S/N > 5$ up to 1 R_e.

3.1.2 Stellar populations, SFHs and characteristic timescales

Fixing the retrieved kinematics from the first step, we run pPXF again, now using a multiplicative Legendre polynomial of degree 7. With this, we correct low-frequency continuum variations. From this second run we obtain the mean stellar ages and total metallicities, but also the SFHs of each galaxy.

As illustration, we present in Figure 3.2 a SFH of a random galaxy in our sample. In this case, the SFH is shown as the 'cumulative' stellar mass that the galaxy assembles with cosmic time. From this, one can compute several characteristic times, such as those times when the galaxy formed the 50% and 90% of their stellar mass (t_{50} and t_{90}, respectively). We also define t_0 as the time at which the galaxy started forming stars, which does not need to correspond to the time of the Big Bang. These ages are shown in Figure 3.2 as red vertical dash-dotted lines. From these times we define the characteristic timescales that can provide information about how the star formation occurred. We define $\Delta_{90} = t_{90} - t_{50}$ and $\Delta_{50} = t_{50} - t_0$, also shown in Figure 3.2. For example, a high value of these parameters is representative of an extended SFH, whereas low values of both would represent very early and fast formation timescales.

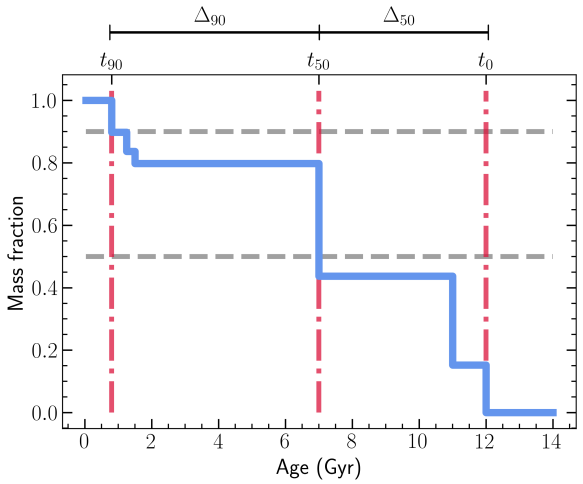

Figure 3.2: Example of a derived SFH using pPXF , corresponding to the galaxy 11954-1902. It shows how the mass fraction of stars is build over cosmic time, since the Big Bang 14 Gyr ago. The steep increments are the result of not applying a regularization in the pPXF routine. Dashed gray lines show the 50% and 90% values of the total mass fraction. Dash-dotted vertical lines mark the position of t_0, t_{50} and t_{90} parameters, which are the times at which the mass fraction surpasses 0%, 50% and 90%, respectively. Based on these parameters, we define the timescales $\Delta_{90} = t_{90} - t_{50}$ and $\Delta_{50} = t_{50} - t_0$ to parametrize the SFH of a galaxy.

The results for the most relevant stellar population properties obtained in this section are also shown in Table 3.1. Moreover, the table also presents the [α/Fe] ratio for these galaxies. They were calculated using line-index measurements following the methodology described in Domínguez Sánchez *et al.* [123] and Ferré-Mateu, Mezcua, and Barrows [77] (value measured by H. Domínguez-Sánchez).

Table 3.1: Kinematic and stellar population results from the analysis of the stacked spectra covering $1R_e$. Stellar velocity, stellar velocity dispersion, age and metallicity are the output of the pPXF analysis [112, 113]. The rotational parameter λ_R is extracted as in Fischer, Domínguez Sánchez, and Bernardi [95], which could not be calculated for a handful of galaxies. The α-enhancement was measured by H. Domínguez-Sánchez. Δ_{50} and Δ_{90} are two parameters that can be used to characterize galaxy formation timescales. The last column corresponds to the galaxy allocation in groups according to the K-Means classification (Section 4).

Plate-IFU	v (km s^{-1})	σ (km s^{-1})	λ_R	**Age (Gyr)**	**[M/H] (dex)**	**[α/Fe] (dex)**	Δ_{50} **(Gyr)**	Δ_{90} **(Gyr)**	**Cluster group**
8443-1901	95.40 ± 0.66	162.69 ± 1.62	0.40	9.03 ± 2.32	0.127 ± 0.043	0.096	3.00	6.50	B
8721-1901	109.00 ± 1.24	206.73 ± 4.28	-	12.96 ± 0.40	0.307 ± 0.017	0.400	0.00	0.00	A
8323-1901	84.76 ± 0.67	178.21 ± 2.38	0.77	10.24 ± 1.31	0.335 ± 0.050	0.079	2.00	0.00	A
9492-1901	117.05 ± 1.00	197.28 ± 2.23	-	13.19 ± 1.02	0.149 ± 0.019	0.348	0.00	0.00	A
9042-1901	106.08 ± 1.17	229.64 ± 5.98	-	12.79 ± 1.11	0.318 ± 0.080	0.274	0.00	0.00	A
7977-1901	91.69 ± 1.29	158.27 ± 5.52	-	11.49 ± 1.27	0.213 ± 0.043	0.151	2.50	0.50	A
9869-1901	99.77 ± 0.85	197.83 ± 3.24	0.19	13.34 ± 0.62	0.388 ± 0.039	0.150	0.00	0.00	A
8601-1902	98.63 ± 0.66	178.83 ± 5.17	0.16	13.62 ± 0.73	0.223 ± 0.077	0.350	0.00	0.00	A
9507-1902	114.46 ± 1.98	291.23 ± 6.62	0.65	13.32 ± 0.57	0.272 ± 0.034	0.319	0.00	1.00	A
8243-1902	106.73 ± 0.86	231.91 ± 5.98	-	13.27 ± 0.87	0.363 ± 0.034	0.200	0.50	0.00	A
8616-1902	89.86 ± 1.47	205.35 ± 6.16	0.67	11.41 ± 1.90	0.293 ± 0.053	0.350	0.00	3.00	A
8486-1902	102.03 ± 0.76	170.74 ± 4.82	0.31	11.91 ± 0.65	0.361 ± 0.047	0.254	2.00	0.00	A
8464-3703	98.71 ± 0.64	190.73 ± 5.18	-	13.83 ± 0.40	0.117 ± 0.078	0.300	0.00	0.00	A
8137-3703	91.22 ± 1.25	143.88 ± 2.89	0.37	6.56 ± 2.39	0.154 ± 0.048	0.100	9.50	0.00	C
10216-3703	98.51 ± 1.50	211.58 ± 5.23	-	13.48 ± 1.08	0.278 ± 0.040	0.400	0.00	0.00	A
10510-1901	100.40 ± 0.67	193.53 ± 4.37	-	12.19 ± 0.67	0.270 ± 0.095	0.400	2.50	0.00	A
11011-1901	71.64 ± 1.59	232.24 ± 5.63	0.57	13.09 ± 0.35	0.362 ± 0.053	0.259	0.00	0.00	A
11020-1902	86.06 ± 0.74	211.87 ± 2.93	0.48	6.74 ± 1.85	0.366 ± 0.059	0.017	0.00	7.75	B
11827-1901	43.96 ± 0.93	165.14 ± 2.35	0.48	6.42 ± 2.48	-0.070 ± 0.099	0.000	3.50	9.25	B
11943-9102	90.56 ± 1.22	251.36 ± 4.47	0.34	13.61 ± 0.56	0.144 ± 0.053	0.265	0.00	0.00	A
11945-1901	100.65 ± 1.28	228.63 ± 5.01	0.67	12.90 ± 0.48	0.325 ± 0.065	0.286	0.00	0.00	A
11979-1902	108.11 ± 1.45	239.61 ± 4.42	0.54	13.34 ± 0.33	0.329 ± 0.032	0.400	0.00	0.00	A
11984-1902	102.40 ± 0.80	141.08 ± 1.93	-	10.33 ± 1.99	-0.137 ± 0.039	0.364	4.50	2.00	B
8248-3704	87.30 ± 0.67	133.57 ± 2.76	0.37	5.59 ± 1.71	-0.006 ± 0.064	0.049	11.50	0.00	C
8710-1902	85.89 ± 1.45	194.65 ± 4.93	-	13.43 ± 0.64	0.207 ± 0.111	0.400	0.00	0.50	A
9496-1902	94.39 ± 1.55	235.65 ± 5.81	-	13.09 ± 0.65	0.234 ± 0.046	0.300	0.00	5.50	A
9880-1902	98.85 ± 0.97	175.18 ± 4.43	0.29	12.82 ± 0.66	0.344 ± 0.068	0.255	0.00	0.00	A
11954-1902	59.35 ± 3.19	135.07 ± 7.13	0.82	5.87 ± 1.33	-0.261 ± 0.123	0.050	5.00	6.20	B
12067-3701	85.46 ± 1.68	114.56 ± 3.28	-	2.96 ± 1.94	0.134 ± 0.090	0.000	12.75	0.45	C
7981-1902	117.84 ± 0.81	164.17 ± 1.33	0.77	4.13 ± 1.52	0.127 ± 0.075	0.000	11.00	1.75	C
11015-1902	104.89 ± 0.62	192.15 ± 3.66	0.29	12.47 ± 0.93	0.337 ± 0.029	0.197	0.00	2.00	A
11960-1902	88.46 ± 1.53	272.57 ± 6.68	0.42	13.26 ± 0.72	0.288 ± 0.041	0.400	0.00	5.50	A
11967-3702	97.18 ± 0.72	197.37 ± 5.49	0.29	13.56 ± 0.33	0.354 ± 0.029	0.400	0.00	0.00	A
11968-1902	81.67 ± 0.98	204.68 ± 4.20	0.62	12.72 ± 0.49	0.352 ± 0.060	0.293	0.00	2.00	A
11969-1902	90.34 ± 0.37	187.18 ± 4.57	0.44	13.21 ± 0.81	0.219 ± 0.054	0.200	0.50	0.00	A
12624-3702	83.60 ± 1.42	218.39 ± 4.53	0.45	13.01 ± 0.63	0.274 ± 0.066	0.300	0.50	2.50	A
12673-1901	101.98 ± 1.10	256.98 ± 4.32	0.52	13.28 ± 3.15	0.236 ± 0.088	0.300	0.50	0.50	A

3.2 IFU analysis

Once we have obtained the global parameters within $1R_e$, which will be discussed in Chapter 5, we also use the datacubes to study in more detail how the relevant properties vary within different regions of the galaxy. For this, we have used in a similar fashion as the steps described above, the pPXF routine. However, in this case we have employed the GIST Pipeline [124], particularly tailored for IFU data. GIST extracts the stellar kinematics and stellar populations on a spaxel basis. This is the same aim of the Firefly VAC (Section 2.1). The stellar population values on this VAC come from a general analysis of the MaNGA sample. As we have denoted, compact galaxies are particularly different from extended local galaxies. This is the main motivation for performing our own spatially-resolved stellar population analysis. Therefore, spaxels were binned to reach $S/N = 20$ per bin, in order to have a better characterization of the spatial properties. This value was chosen after several trial and error attempts, aiming to minimize the required S/N with the scattering of the resulting profiles. Note that when forming a bin, we increase the S/N ratio at the expense of losing spatial resolution.

The original code was adapted to run with MaNGA cubes. With this pipeline, we obtained our own spatially-resolved stellar populations and kinematics, similar as in Firefly, but tailored to our sample of compact galaxies.

4 Analysis: galaxy clustering

Coupling the information of the mean age of the galaxies with the timescales can be a powerful tool to understand when and how fast these compact galaxies were formed. We present in the left-side plot in Figure 4.1 the Δ_{90} and Δ_{50} values for each galaxy, color-coded by its mean age, as obtained in Section 3. As we have not applied any regularization in the pPXF analysis, the SFHs are similar to the one presented in Figure 3.2, bursty and not smooth. This makes it more likely for galaxies to have the same Δ values. We have thus introduced a small gaussian shift to these values only for illustrative reasons in the figure.

The location of the galaxies within this figure can provide information about the different formation channels they have undergone. For example, relic galaxies, which are expected to form very early and extremely fast, almost in a single-like star formation burst, are expected to be located in the lower right corner of Figure 4.1, i.e. with both small Δ_{90} and Δ_{50}, representative of a steep SFH. On the contrary, younger galaxies with more extended SFH will show larger Δ_{90} and/or Δ_{50} values.

In addition, when looking at the derived SFHs and stellar populations of the 37 galaxies in our sample, we notice that there are different trends. We thus want to investigate whether we can group the compact galaxies based on their stellar populations. These groups should consist of galaxies with similar SFHs, so that they represent similar formation processes. A computational algorithm was used to consider all the stellar population variables, as this classification would be multidimensional and quite complex. Because our sample is small (37 objects) applying Machine Learning is not feasible. We have instead used a K-Means algorithm from the `sklearn` Python package[1]. The algorithm allocates each of the 37 compact galaxies to one of the K number of clusters set previously. The classification depends on the properties of each galaxy, grouping the most similar ones. In particular, we wish to focus on the SFH parametrization classification, therefore we have not introduced any kinematic parameter in the analysis, nor any size constraint at first.

The properties considered by the algorithm are: Δ_{90}, Δ_{50}, Age, [M/H], $\Sigma_{1.5}$, and $M_\star$. We arranged galaxies in three main groups[2]. The mean values of the centroids in each parameter space and the number of galaxies in each group can be found in Table 4.1. The algorithm gave more weight to Δ_{90}

[1] `https://scikit-learn.org/stable/modules/generated/sklearn.cluster.KMeans.html`

[2] Although the elbow method sets the optimal number of clusters to 5, we have decided to use K=3 given the small number of galaxies to be considered. K=3 maximizes the differences between groups while keeping enough number of galaxies in each cluster for statistical analysis.

Table 4.1: Centroid position for the $K = 3$ clusters in the K-Means classification. Each column represents the position in the respective dimension for the parameters used in the process. In the last column we denote the number of galaxies in each group.

	Δ_{90} (Gyr)	Δ_{50} (Gyr)	Age (Gyr)	[M/H] (dex)	$\log \Sigma_{1.5}$ (dex)	$\log(M_\star/M_\odot)$ (dex)	# galaxies
Group A	0.82 ± 1.54	0.39 ± 0.78	12.89 ± 0.78	0.282 ± 0.071	10.41 ± 0.08	10.51 ± 0.24	28
Group B	6.34 ± 2.42	3.20 ± 1.75	7.68 ± 1.71	0.005 ± 0.220	10.51 ± 0.16	10.61 ± 0.19	5
Group C	0.55 ± 0.72	11.19 ± 0.72	4.82 ± 1.37	0.102 ± 0.063	10.49 ± 0.10	10.56 ± 0.21	4

and Δ_{50} in the classification, where a group division is clearly seen. Other stellar population parameters, like metallicity, were used to allocate galaxies with intermediate Δ_{90} and Δ_{50} values.

We have shown in Table 3.1 the group each galaxy belongs to according to this clustering algorithm. We also show the clustering results in the right plot in Figure 4.1. Similar to the left panel, here we plot the Δ_{90} vs. Δ_{50}, but now differentiating the 3 groups from the K-Means classification, shown by different shade of green and symbols. The location of these three groups suggests that each group can be representative of the different formation pathways proposed for compact galaxies, as we will further discuss in Chapter 5.

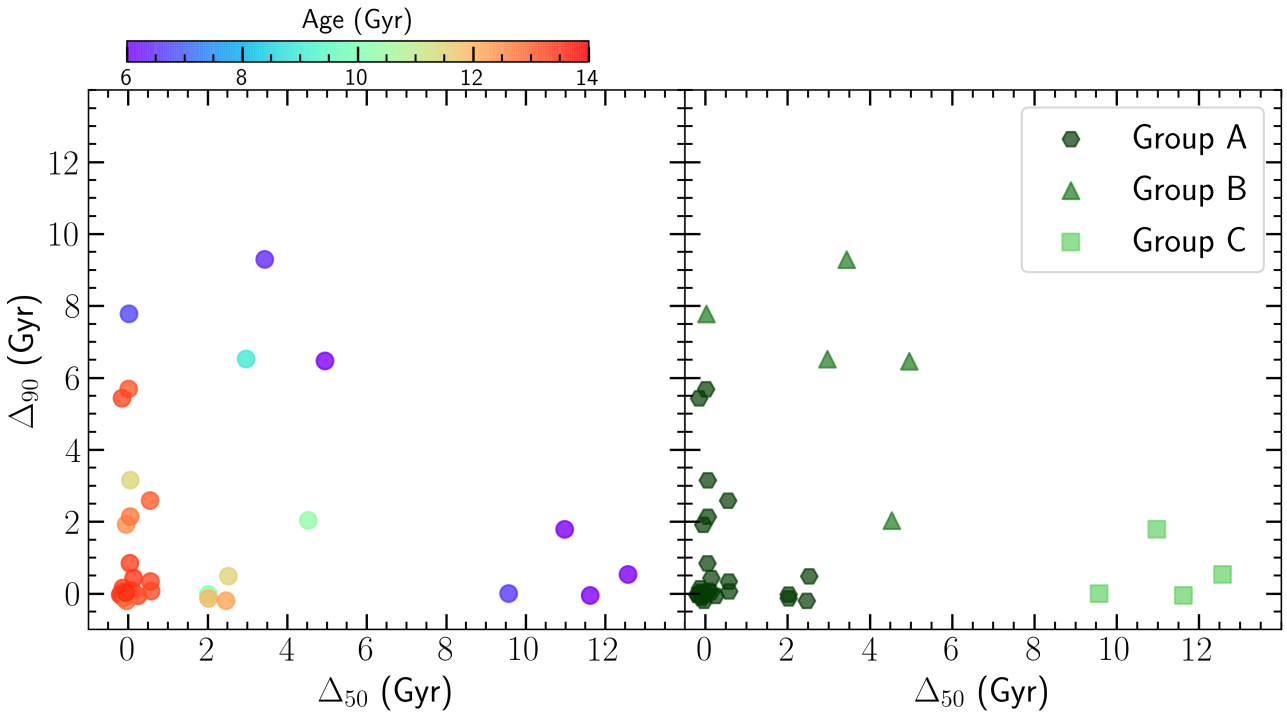

Figure 4.1: Characteristic formation timescales of compact galaxies in our sample. *Left:* Each galaxy is colored according to its derived mean age within 1 R_e. The values have been randomly shifted to avoid overlapping points. This summarizes when and how fast a galaxy has formed its entire stellar mass. The different locations within this plot can help characterize different formation pathways. The oldest galaxies are clustered towards very short formation timescales, while youngest ones show larger values in one of the timescales. *Right:* Same as in left panel, but with galaxies colored and different symbols according to the results of the K-Means clustering algorithm. We label each group as described in the text.

We average the SFHs of each class from the K-Means classification to confirm whether they show distinctively different SFHs. It is shown in Figure 4.2, as the solid line, colored according to each class. The shaded regions show the standard deviation for each SFH. As in Figure 3.2, dashed lines show the 50% and 90% of the total mass. Group A galaxies are generally formed in an extremely fast and early

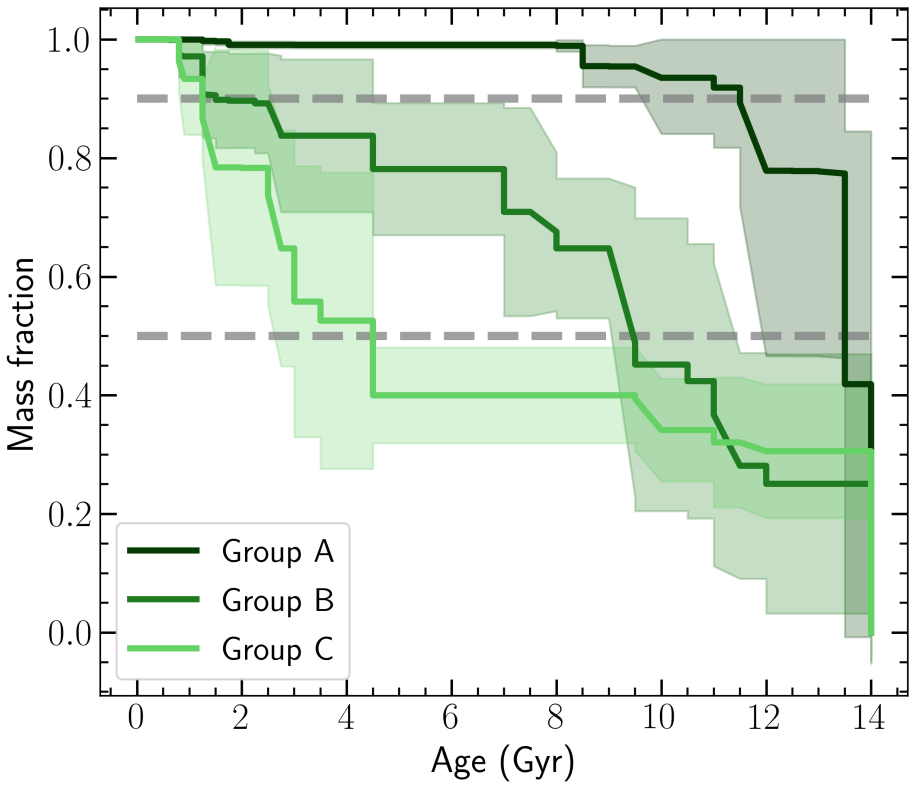

Figure 4.2: Mean SFH for each class of the K-Means classification. The shaded region corresponds to the 1σ deviation error. Dotted lines show the position of the 50% and 90% of the total mass fraction. Distinctive SFHs are seen for each class.

star-forming event, while both Group B and Group C galaxies show a more steady mass assembly, with Group C being younger than Group B. Overall, Figure 4.2 shows clear differences between the classes, reinforcing the credibility of the K-Means classification.

According to the K-Means classification (Table 4.1 and Figure 4.2), galaxies from our sample of compact galaxies can be neatly classified in 3 groups with distinctively different general properties:

- Group A: The majority of our compact galaxies, 76% of the total sample, belong to this group. They are old galaxies ($>$ 12 Gyr), with extremely steep SFHs ($\Delta_{90},\ \Delta_{50} \sim 0$). They formed in a single burst-like star formation event. Relic galaxies would be found in this group. This group also includes galaxies with slightly younger ages, of $\sim$ 10 Gyr, with steep SFHs as well. These could be the 'late bloomers', i.e. red nuggets that started their formation at later times.

- Group B: Includes a rough 13% of our compact galaxies. They are intermediate-age galaxies with non-extreme formation timescale values. Their SFHs are typically extended over time, forming stars until recently. These would be the best candidates for the true low-mass end of ETGs.

- Group C: With an 11% of the compact galaxy sample, it is the least populated group. This group hosts the youngest galaxies ($\sim$ 5 Gyr), which show two main star-forming episodes: one at early times ($t \sim$ 14 Gyr), which formed roughly the 40% of their stellar mass, and a later one around

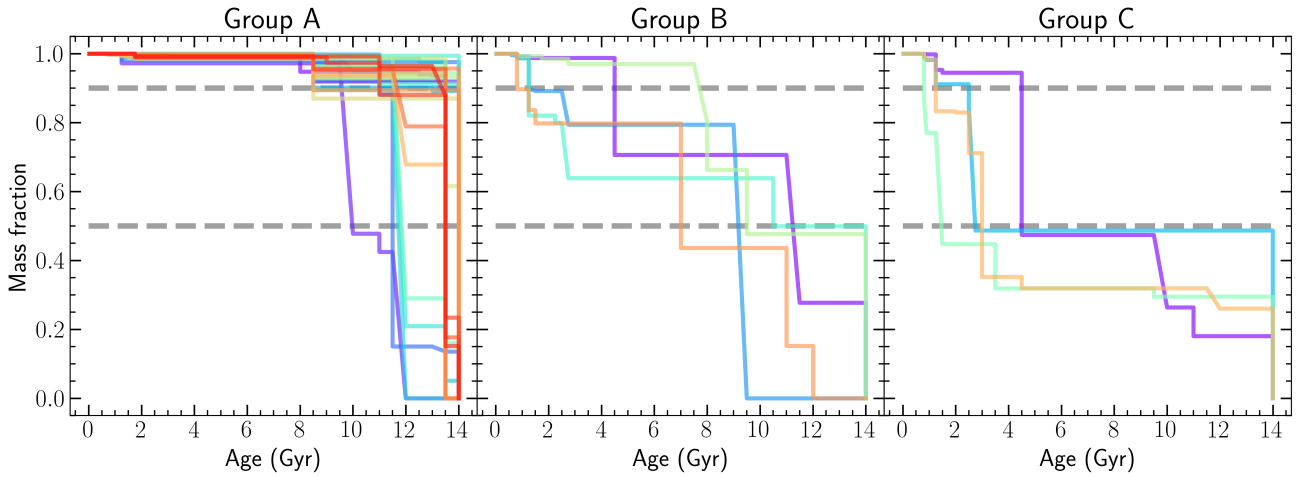

Figure 4.3: Star formation histories of each selected compact galaxy. The left panel shows the SFHs of Group A galaxies. Group B galaxies are shown on the central panel and the right plot includes Group C galaxies. As in Figure 3.2, the horizontal dashed lines show the 50% and 90% of the total mass. Clear differences are seen between the SFHs of galaxies in each group, as already hinted in Figure 4.2.

$t \sim 4$ Gyr ago and down to recent times. This is representative of high Δ_{50} values but low Δ_{90} ones. In this case, these could be galaxies that experimented a recent interaction.

As a matter of completeness, we show in Figure 4.3 the SFHs of our 37 compact galaxies, arranged by groups. Overall, Figure 4.3 again reinforces that the galaxy classification succeeded. In the following section we will further investigate the global properties of each class and discuss them within the wider context of galaxy evolution.

5 Discussion

5.1 Bridging the gap of compact galaxies

In the previous chapter we have sketched why the three different groups can be representative of different galaxy formation channels. In the following section we compare the stellar population properties of our 37 compact galaxies with other known compact galaxies. We will use samples of compact massive galaxies and compact ellipticals. We expect to see how different properties of compact galaxies scale with stellar mass. Moreover, we can also be able to confirm whether the groups are truly illustrative of distinct formation pathways.

5.1.1 Insights from the stellar populations

In this work we have used the mass-size relation to select the compact galaxies in the MaNGA sample. The mass-metallicity relation (MZR) is also one of the most tight relations known followed by galaxies, whereby more massive galaxies tend to be more metal rich, e.g. [125–131]. The location within this relation can give much insight into the formation processes of the galaxy. We therefore define a kind of fundamental plane for compact galaxies, namely the stellar mass-metallicity-effective radius plane. This is shown in Figure 5.1 along with each projection. We show the 37 compact galaxies in our sample, a sample of cEs from [35, 72], and CMGs from [53, 54, 58, 64, 110, 132].

The top-right projection in Figure 5.1 depicts the stellar mass-size relation. This projection was already visited in this work (Figure 2.1). In this case we can confirm that our compact galaxy sample effectively fills the gap between cEs and CMGs, as suggested by Ferré-Mateu *et al.* [35]. This reinforces the success of the compact galaxy selection and its criteria (see Section 2.2). On the other hand, the bottom-left projection shows the metallicity-size plane. As seen in the stellar mass-size projection, CMGs are bigger galaxies than cEs. However, each family has important dispersion in the metallicity space, which prevents to extract clear conclusions from this projection.

In the mass-metallicity plot, we show the Gallazzi *et al.* [133] relation for ETGs at $z \sim 0$. This relation can reveal important information about the formation processes of galaxies. In general, in galaxies with an external origin a higher metallicity is expected as they were once more massive. Stripping would have partially removed some of their stars, thus becoming compact, but the remaining stars would have kept the original metallicity. Therefore, this type of objects are expected to be outliers in the MZR. On the contrary, galaxies that have formed following in-situ processes, will follow the MZR (or at least

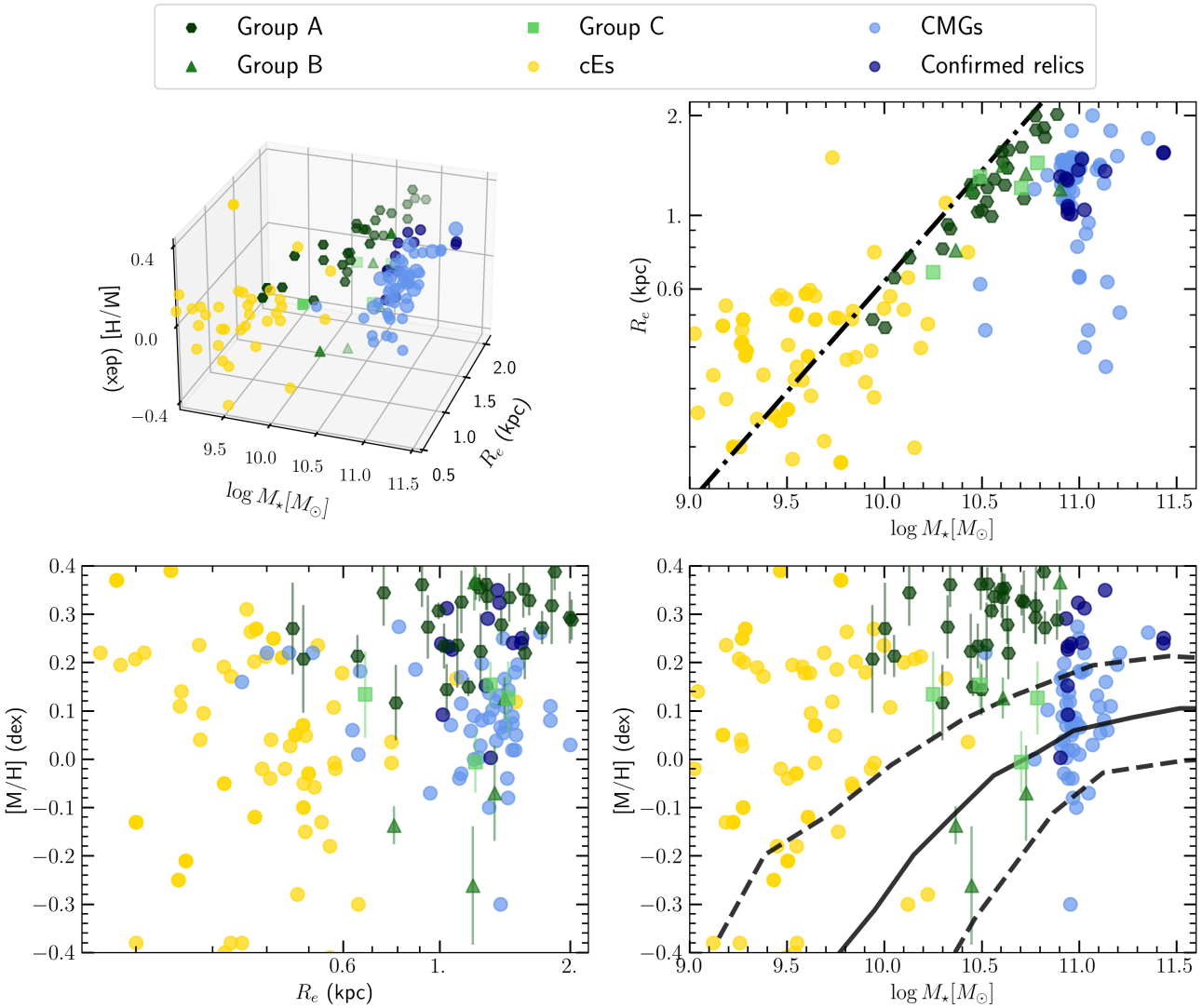

Figure 5.1: Stellar mass-metallicity-radius fundamental plane. Yellow dots show the values of low-mass cEs from [35, 72, 79]. Blue dots show the CMG values from [53, 54, 58, 64, 110, 132], where darker blue dots show the current confirmed relics. Galaxies are labelled according to their classification using the K-Means algorithm. The projections of the fundamental plane are schemed on the right plots. The dash-dotted line in the mass-size plot shows the compactness limit adopted in this work, as in Figure 2.1. The mass-metallicity relation at $z \sim 0$ from Gallazzi *et al.* [133] is shown as a dashed line in the corresponding plot, where the solid line shows the median value of the fitting and the dashed lines the 16% and 84% percentiles.

be within its intrinsic scatter). Galaxies like relics are expected to also host relatively high metallicities and thus be outliers, as the total metallicity decreases during the second phase, which they avoid.

In this projection, cEs present the largest deviations from the MZR, the majority being outliers of it. It has indeed been shown that those deviating the most from the relation formed following external processes [35]. However, there is a small fraction of cEs that are closer to the scaling relation (or within the scatter), and thus they have been proposed to have an intrinsic origin [35, 71, 72, 80]. On the other hand, CMGs follow in general the MZR of massive galaxies, with a scatter compatible with the intrinsic one of the relation. For those that are confirmed relics, these are mostly outliers of the relation, as explained above. They show more elevated metallicities than the non-relic CMGs and normally sized ETGs, due to having missed the second phase that decreases the galaxy total metallicity.

We find that the compact galaxies from this work show a variety of properties in this relation. Group A compact galaxies are clear outliers to the MZR, being much more metal-rich than the non-compact ETGs. This is compatible with the steep SFHs and old stellar populations shown by some galaxies in this group. These could be good candidates for intermediate-mass relic galaxies.

The MZR is best followed by Group B galaxies. This agrees with their continuous and extended SFH, as the newborn stars should follow the current MZR, suggesting an intrinsic origin. In Figure 5.1 we see that Group B galaxies appear even less metallic than described by the Gallazzi *et al.* [133] relation. Finally, Group C galaxies appear in the limiting region between being outliers and the intrinsic scatter of the MZR. Based on their SFHs, they have recently resumed star-forming processes. With their position in the stellar mass-metallicity plane we guess that these galaxies could be the result of a stripping process. The stripping event would have triggered the recent star-forming activity. Overall, these analyses are based on the overall behavior shown by each group. The small number of galaxies in each group (specially in Group B and Group C), prevents us to state solid relations. Each galaxy should be revisited individually to sketch their particular formation channel.

There is one extreme outlier from Group B. This galaxy is also the one with the highest mass, 11020-1902, which followed the mass-size relation of $z \sim 2$ galaxies in Figure 2.1. The galaxy particular SFH is represented in blue in the central plot of Figure 4.3. In Figure 4.1 we see that this galaxy is the only in Group B that has $\Delta_{50} \sim 0$ but very large Δ_{90}, with intermediate stellar ages (~ 8 Gyr). The initial hypotesis was that this could be the best candidate for a relic galaxy, but the recovered SFH does not fully support this.

One possibility to explain the origin of this galaxy is if it is a 'late-bloomer' [35, 58]. These are galaxies that followed the formation pathway of massive galaxies, but that started forming stars much later in cosmic time. 'Late-bloomers' will thus have intermediate ages ($\sim$8-10 Gyr) but very short Δ_{50}. If their Δ_{90} is also small, then these could be the replica of the massive relic galaxies. In fact, we see that only one galaxy in Group A shows small Δ_{50}, Δ_{90} and intermediate ages: 8323-1901, whose SFH is depicted in purple in the left plot in Figure 4.3. However, if the 'late-bloomer' suffers stripping processes, these would trigger star-forming events, increasing the value of Δ_{90}. This would be the case of 11020-1902, featuring $\Delta_{50} \sim 0$ and large Δ_{90}.

Another interesting parameter that can help to classify galaxies is the [α/Fe] ratio. This value is deeply related to stellar formation processes. A high [α/Fe] ratio is representative of a quick star-forming episode, almost single-burst like, while low [α/Fe] values are related to more extended SFHs [18–21]. [α/Fe] values were provided by H. Domínguez-Sánchez and are measured on the stacked spectra at 1 R_e following the methodology from Domínguez Sánchez *et al.* [123]. In short, this is based on the measurement of absorption line strengths (Mgb, Hβ, Fe5270, Fe5335) and their comparison with single stellar population synthesis models. We present in Figure 5.2 the [α/Fe] distribution values of our compact galaxies, compared with those from the literature sample of cEs and CMGs. Group A galaxies show the highest [α/Fe] values. Their high [α/Fe] values are consistent with their early and steep SFHs (see Section 5.1). Such high [α/Fe] values are similar to those from CMGs, even slighlty higher in some

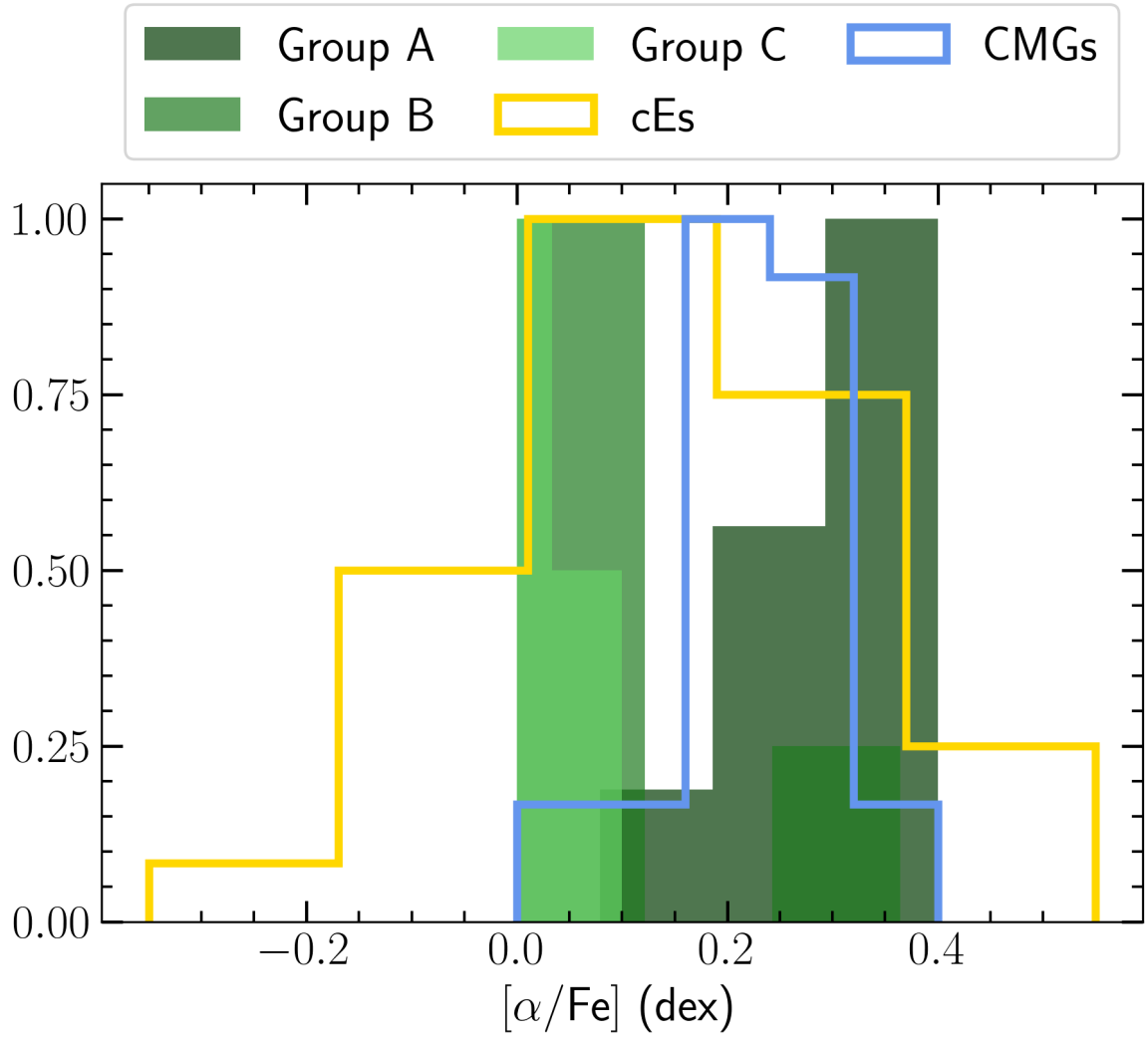

Figure 5.2: [α/Fe] distributions of the 37 selected compact galaxies. Each group histogram is colored accordingly. The yellow and blue solid lines show distributions of a sample of cEs [35, 72] and CMGs [53, 55, 58, 110], respectively. We do not include the confirmed relics in the CMG sample. Each bar is normalized by the maximmum number of counts of that sample.

cases. On the other hand, Goup C and Group B show lower [α/Fe] values, compatible with their more extended SFHs. cEs show the largest dispersion of [α/Fe] values, indicative of the mix origin they have.

5.1.2 Insights from the stellar kinematics

We just have seen that stellar populations can provide interesting clues about the origins of the compact galaxies found in the local Universe, based on known scaling relations. Similarly, we can use kinematic relations to compare the properties of our compact galaxies with those at different masses and see how they relate. One interesting relation is the velocity dispersion-mass relation. These two parameters seem to relate well as a power law, showing a break at $\log(M_\star/M_\odot) = 10.26$, which is reported by several authors, e.g. [134–136]. This relation has been found to have a narrow intrinsic scattering, despite this break [137–140]. That is, stellar mass and velocity dispersion are strongly correlated, despite their apparently distinct origins: stellar mass is related to the SFH of the galaxy while velocity dispersion is a kinematic parameter.

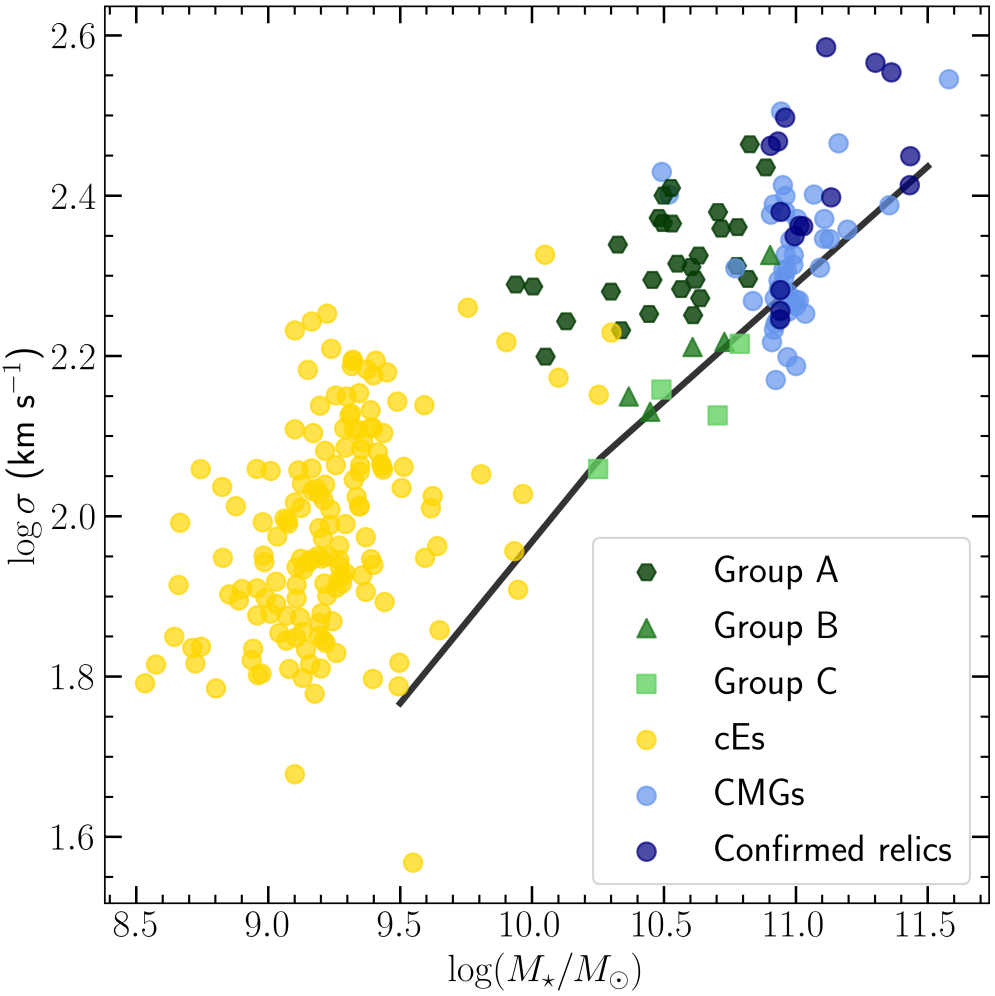

Figure 5.3: σ-stellar mass for compact galaxies. Our selected 37 compact galaxies are green-colored and with symbols according to the K-Means classification. Yellow dots show the position in the plane of the cEs from [35, 54, 80]. Blue dots show the CMGs from [53, 54, 58, 64, 110, 132], being the dark blue ones the corresponding to confirmed relics. The solid black line shows the σ-stellar mass relation from Zahid *et al.* [140], which has minor scattering. However, compact galaxies appear as outliers from the trend.

The σ-stellar mass relation was used in the INSPIRE survey first data release [55]. This is a recent and ongoing project aiming to identify and categorize relic galaxies in the local Universe. Their unexpected result was that relic galaxies tend to deviate from the σ-mass relation, and that this deviation depends on how extreme their properties are [64]. Relic galaxies with more extreme SFHs featured higher σ values.

We show in Figure 5.3 the σ-stellar mass for our selected compact galaxies and the cEs and CMGs samples from the literature. Even though previous works report that the σ-stellar mass relation has low intrinsic scattering, we see that compact galaxies present clear deviations from the trend. The overall outlook reveals that the number of compact galaxies following the σ-stellar mass relation increases with stellar mass. Only a handful of cEs seem to fit with the Zahid *et al.* [140] trend. The vast majority of considered cEs show higher velocity dispersion than predicted. At the high-mass end, there is a larger number of CMGs that appear to obey the σ-stellar mass relation. However, there is also a considerable amount of CMGs that are still outliers. As found by Spiniello *et al.* [64], CMGs with the highest deviations are generally extreme relics.

Considering our compact galaxies, they seem to follow this description. The region around the Zahid *et al.* [140] relation in the mass range of our compact galaxies is more populated than the corresponding region in the cE family but less populated than that of the CMGs. Group A galaxies present the highest velocity dispersion among our compact galaxy sample, being outliers of the local scaling relation. They have velocity dispersion similar to most CMGs and some relic galaxies. Given that most of their stellar populations properties are also similar to these more massive galaxies, this suggests that a relation between these families is plausible. On the other hand, both Group B and Group C galaxies follow the trend from Zahid *et al.* [140]. Given their more extended SFHs, this is a further confirmation that these compact galaxies can truly be the low-mass end of ETGs.

There appears to be a dichotomy in the kinematics of ETGs: fast rotators (FR) and slow rotators (SR). A fast-rotating galaxy shows a uniform rotational pattern in the innermost regions of their kinematic maps, e.g. [141–144]. Fast-rotators are oblate ellipsoids. On the other hand, the kinematic maps of slow-rotating galaxies can show either no rotation or complex features, e.g. [141, 143, 144]. These galaxies are usually more massive and rounder than fast rotators. From the simulations of Naab *et al.* [145] it was shown that compact galaxies are more prone to be FR.

The λ_R-ε plane is commonly used to kinematically classify galaxies between FR and SR. We show in Figure 5.4 such plane for our 37 compact galaxies. The background is colored to illustrate the density of LTGs (blue) and ETGs (red) galaxies of the whole MaNGA DR17 sample (values were calculated as in Fischer, Domínguez Sánchez, and Bernardi [95]). The Emsellem *et al.* [146] line sets the limit between fast-rotating and slow-rotating galaxies. As before, we also show the sample of cEs and CMG from the literature.

Both CMGs and cEs are, overall, fast rotators. We find that the compact galaxies in our sample are also fast-rotating galaxies. They all show, however, a wide range of both λ_R and ε. Those with smaller λ_R and smaller ε show similar distributions to literature cEs, while those with larger λ_R and ε do not resemble to any other compact galaxy, which could indicate that their progenitor was a massive LTG.

5.2 2D maps and radial profiles

The main advantage of IFU technology is the capability to get spatially-resolved information of the observed objects. In the previous sections we have grasped how the properties of our compact galaxies compare with those of compact galaxies with higher and lower mass. We can take the raw MaNGA datacubes and make a similar analysis of the kinematics and stellar populations, analyzing a spectrum for each spatial element, thus building a 2D property map. With this, we will be in able to get a more detailed insight into the properties of compact galaxies, to help us better understand how they formed.

For this exercise, we employ the GIST Pipeline instead of using the already published maps (e.g. MaNGA Firefly VAC, Section 2.1). This is because we aim for a particular analysis tailored to compact galaxies. By applying this pipeline we are able to tune the parameters of the analysis aiming to get the maximum S/N per bin while keeping acceptable spatial resolution. The GIST Pipeline analyses the

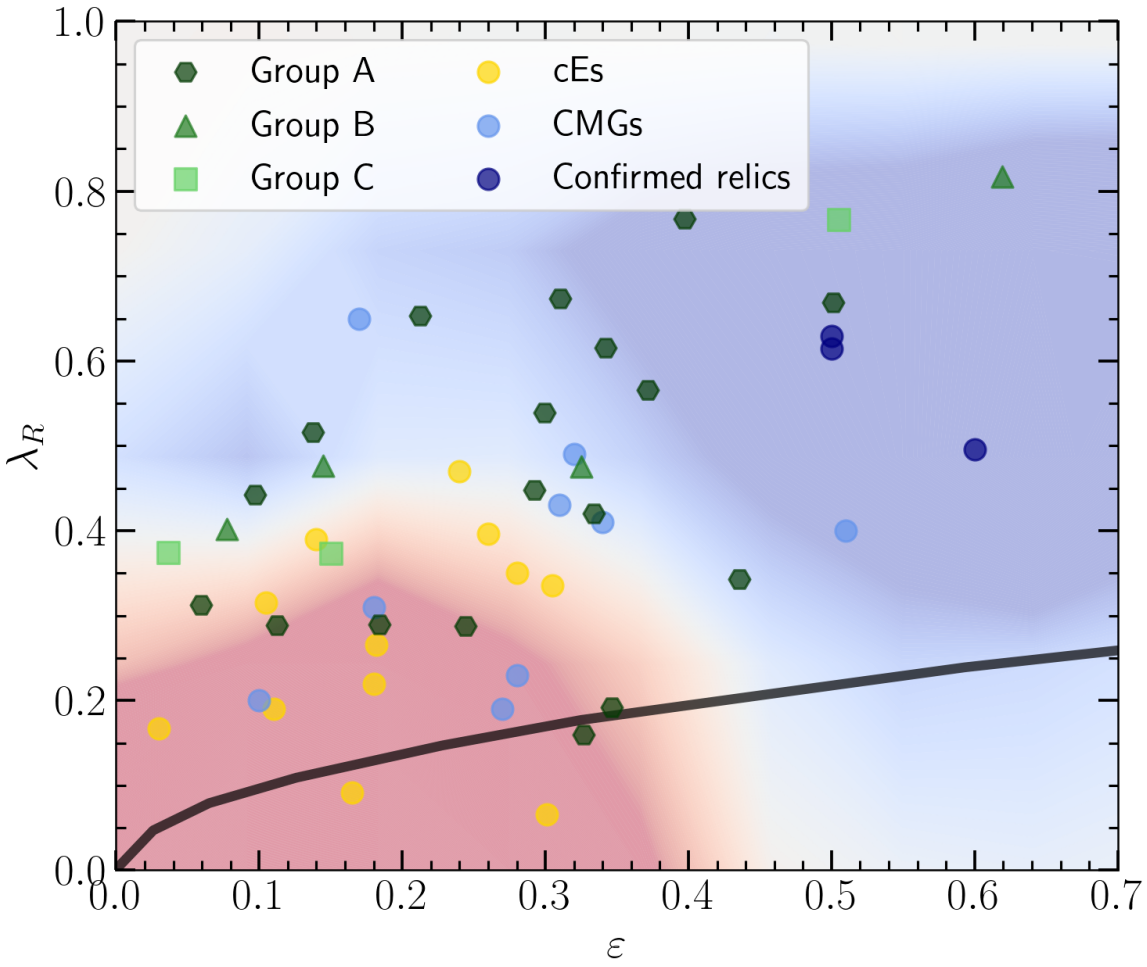

Figure 5.4: $\lambda_R - \varepsilon$ for the 37 selected compact galaxies. Values of λ_R are calculated within 1 R_e, following the description in Fischer, Domínguez Sánchez, and Bernardi [95], which also provides the ellipticity values. Literature cEs and CMGs are also shown as in previous figures. Background colors show the density of ETGs (red) or LTGs (blue), according to the values from Fischer, Domínguez Sánchez, and Bernardi [95]. The solid black line represents the Emsellem *et al.* [146] relation to classify fast-rotating and slow-rotating galaxies. Galaxies below this line are considered SR and above it lie the FR. The main remark is that the vast majority of compact galaxies are FR.

spectrum for each bin in the galaxy using the pPXF routine. We can thus build a property map with the retrieved properties for each spatial element. We refer to Section 3 for more information on these analyses. The Firefly stellar populations catalog was used as double-check of the following analysis.

We show in Figures 5.5-5.7 the stellar population maps of a representative galaxy of each group. 11967-3702 is a Group A galaxy showing old and uniform stellar populations, along with supersolar metallicities. 8443-1901 is a representative galaxy of Group B, showing intermediate ages ($\sim$ 10 Gyr) almost everywhere. In particular, this galaxy shows nearly solar-like metallicities. Finally, 12067-3701 is a Group C galaxy. It features a young core ($\sim$ 7 Gyr) with a surrounding old annulus. The three chosen galaxies appear to have similar values for the [α/Fe] ratio, being fairly higher in 11967-3702. This is in agreement with their SFHs.

We would like to highlight that the analysis related to the 2D maps is work in progress so the results should be taken with care. However, it is clear that much insight can be gained from the detailed study of the spatially resolved properties of galaxies. We plan on carrying a detailed study for each galaxy

group. With this, the final aim is to unveil the formation pathway of each selected compact galaxy.

After visually inspecting the 2D maps, we can plot the radial profiles of their properties to have a more clear view of the differences among compact galaxy groups. We show in Figure 5.8 the radial profiles for age, metallicity and the [α/Fe] ratio for the 37 selected compact galaxies, separated in their corresponding group. In this case, the [α/Fe] ratio is the result from the pPXF algorithm, based on the full spectral fitting. However, the [α/Fe] values used in the previous sections were calculated from the line indices. We have taken the mean of the values of bins within successive $0.25R_e$ rings. For those galaxies for which we could form only 6 rings or fewer, we took radial rings of $0.1R_e$, increasing the significance of the profile data.

Group A galaxies show old stellar populations in the innermost radii, some decreasing towards intermediate ages as we move outwards. Some in this group show flat radial profiles. Overall, the properties of some Group A galaxies seem to be similar to those of confirmed relics [54] and simulated relics [147], characterized by their uniformly old ages.

Group B galaxies show intermediate-age stellar populations, as shown by their mean SFH of Figure 4.2. We see that the ages of most of these galaxies show a positive radial trend, with ages lower at the center than in the outskirts. Group C shows a variety of profiles, representative of the different formation processes of this group.

For those galaxies with a positive age gradient, this can be understood as a cold gas inflow triggering the recent star formation episode in the center of the galaxy. This might occur during a stripping event if there are gas-rich galaxies involved.

Metallicities quickly decrease as we move towards the outskirts. This is a common profile for both massive ETGs [148] and compact galaxies [35, 54]. This trend is seen in the three groups. There are a small group of galaxies, in Group A, where this property seems to be rather constant. Concerning the α-enhancement, only Group A galaxies show really high [α/Fe] values in the central part. In these galaxies, the [α/Fe] values decrease and reach a quite steady value at [α/Fe] ~ 0.2. We can note that all Group B galaxies show an increasing [α/Fe] trend. This is also seen in most Group C galaxies. At the outermost parts, the [α/Fe] ratio of all galaxies seems to fit around [α/Fe] ~ 0.2, regardless of its group.

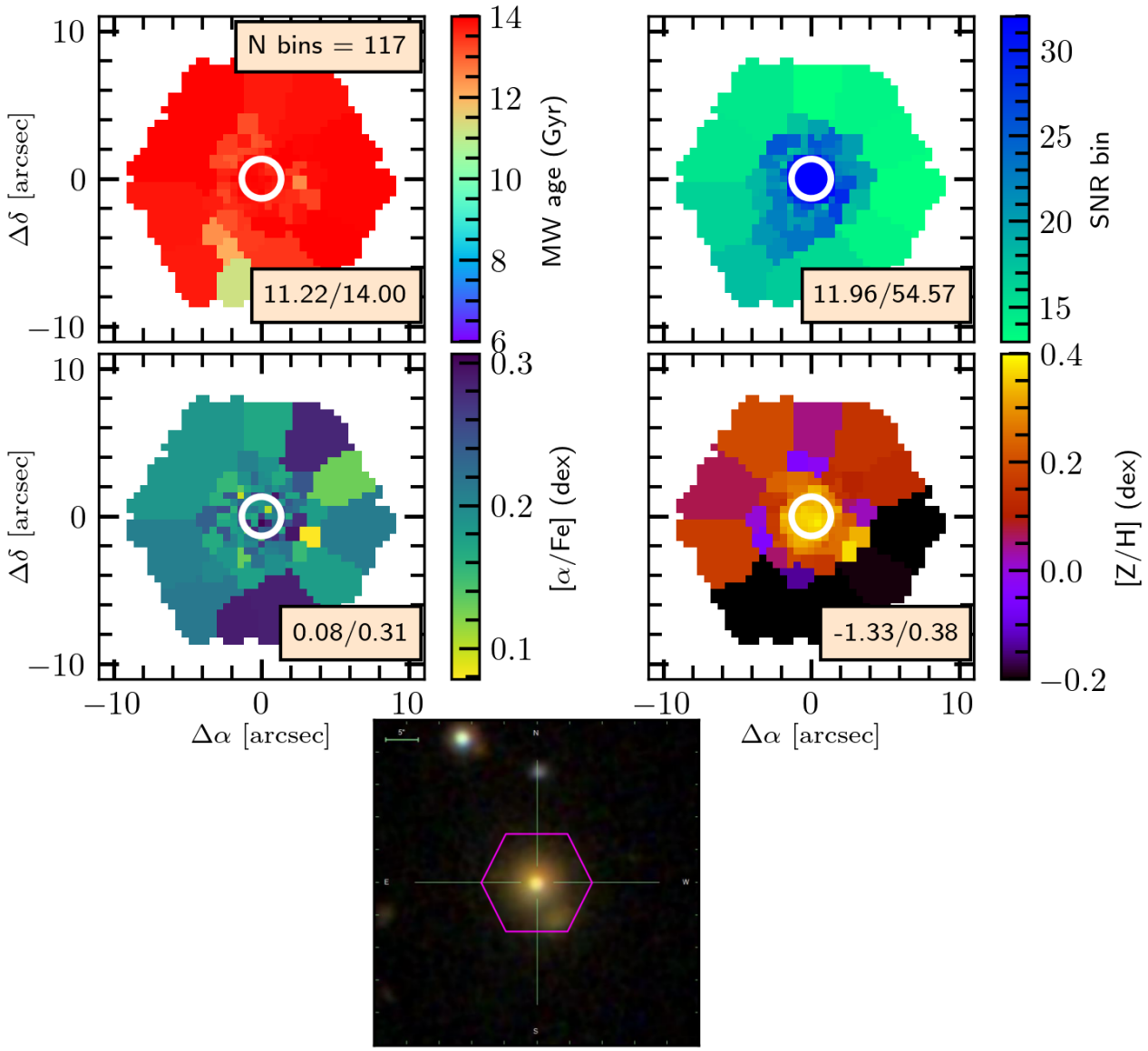

Figure 5.5: Spatially-resolved stellar population maps for 11967-3702, a Group A galaxy. We represent the mass-weighted age, the S/N ratio per bin, the [α/Fe] line strengths and the total metallicity maps in the first and second rows. White circles represent the 1 R_e of each galaxy, which has been circularized. The beige boxes in each image show the minimum and maximum values of the bins. In the upper-left image we denote the number of bins in the galaxy maps. We also provide its MaNGA optical image of each galaxy at the bottom image. The pink hexagon depicts the MaNGA IFUs scope, i.e. the region within we can get the maps. The green colorbar in the bottom image depicts the size of a 5 arcsec projection.

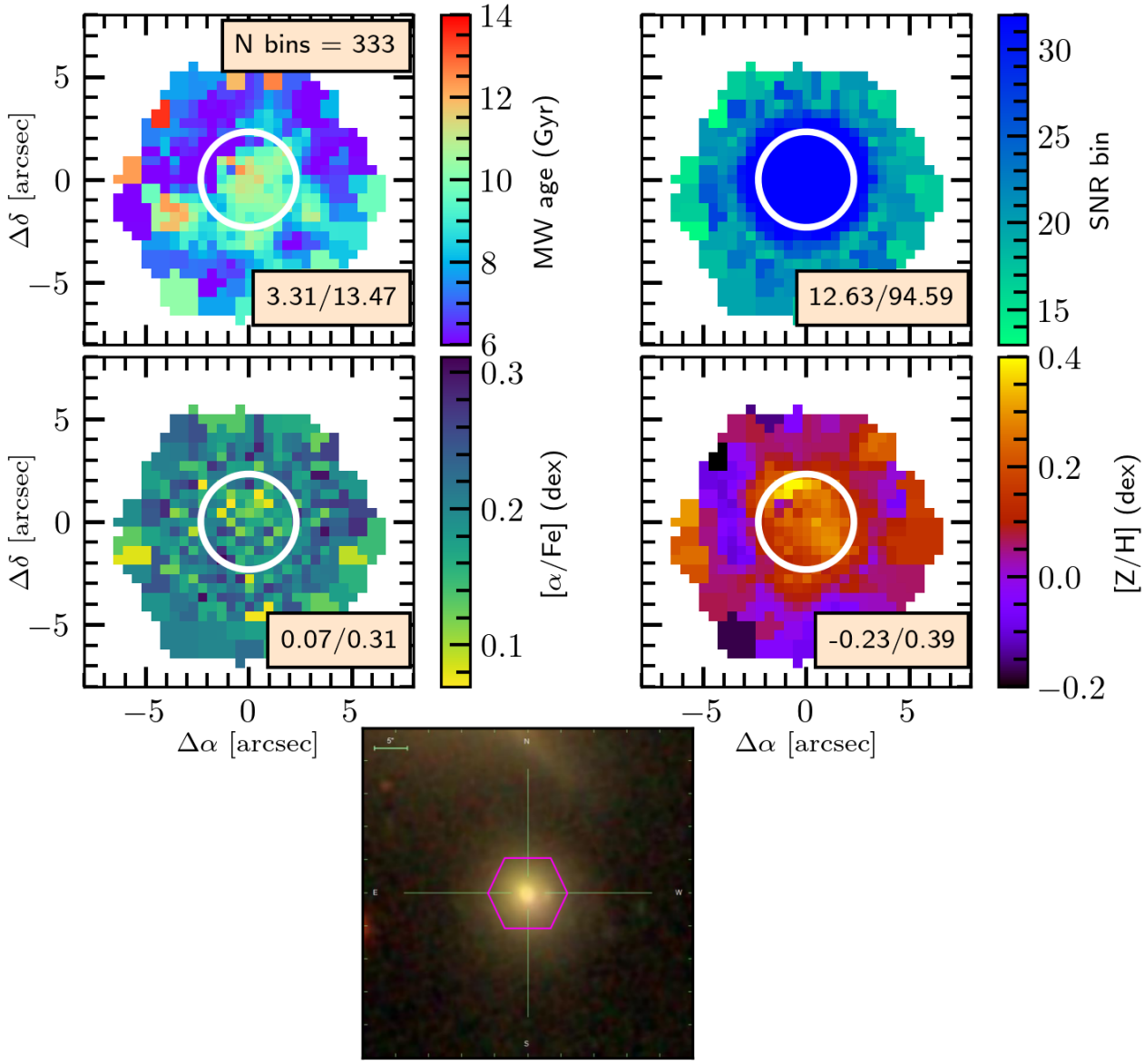

Figure 5.6: Same as in Figure 5.5 but for 8443-1901, a Group B galaxy.

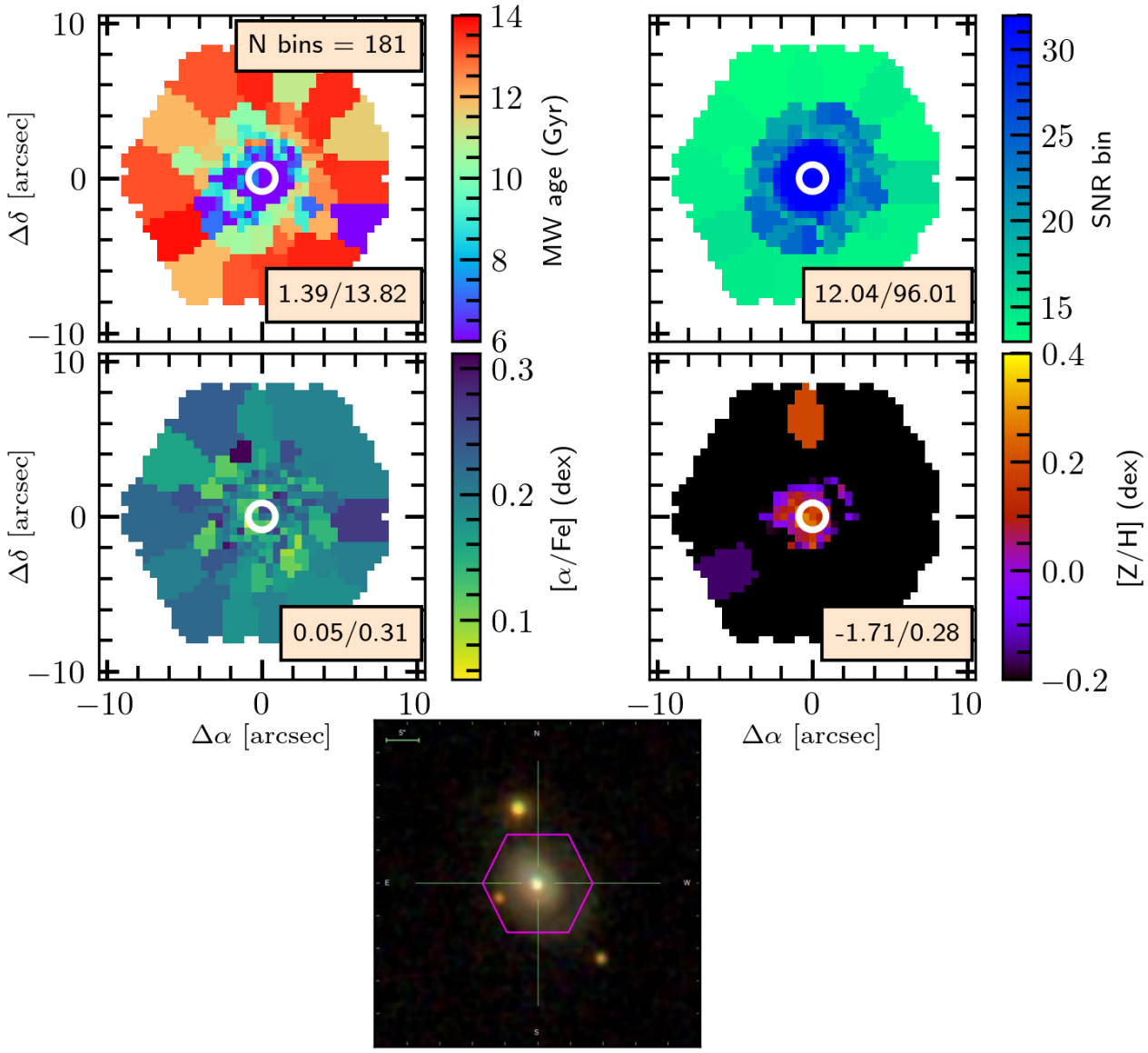

Figure 5.7: Same as in Figure 5.5 but for 12067-3701, a Group C galaxy.

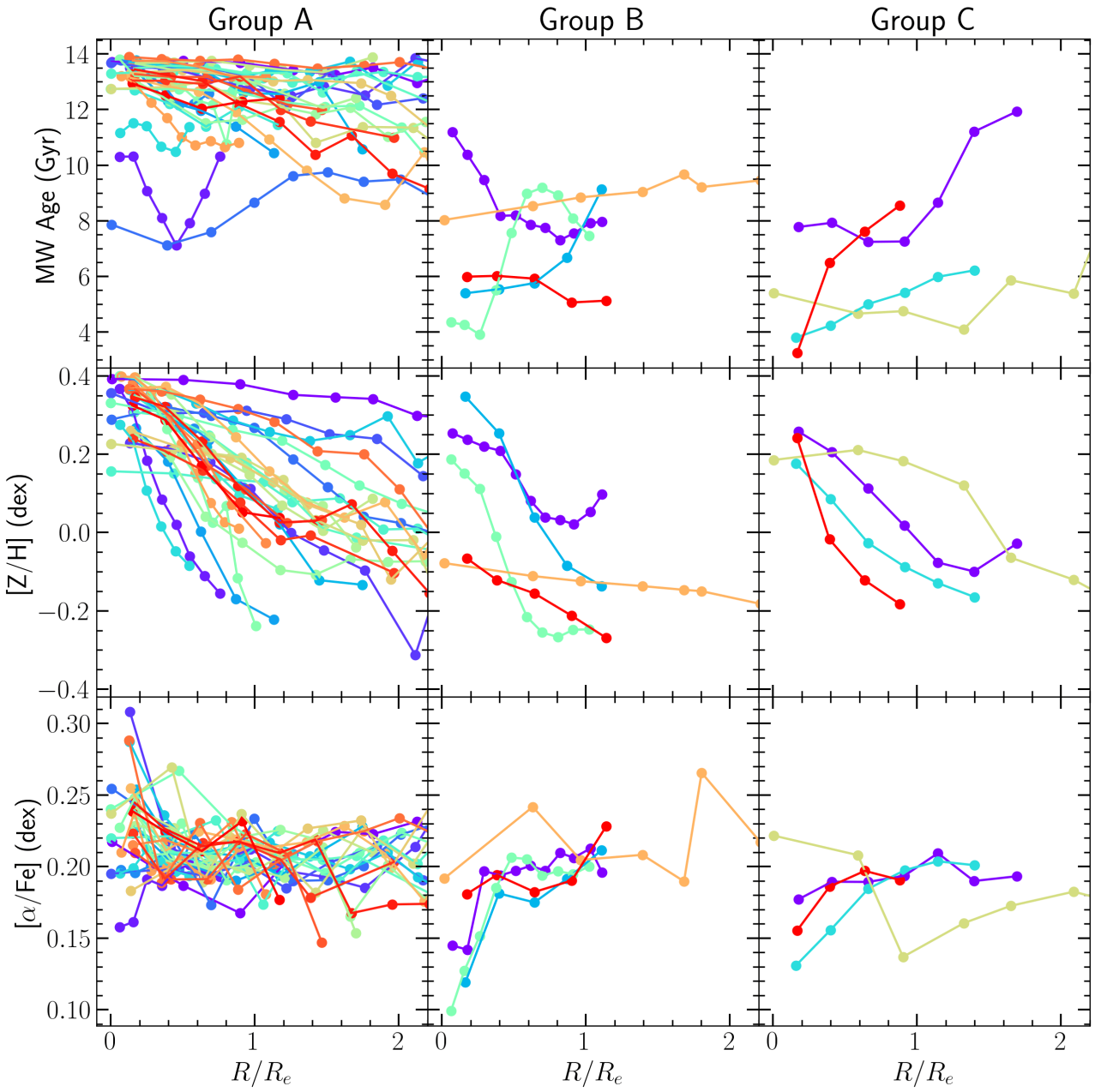

Figure 5.8: Mass-weighted age, metallicity and [α/Fe] radial profiles for the selected compact galaxies in each group. The colors are the same as in Figure 4.3. Clear differences in the radial trends are seen, further reinforcing their different formation processes.

6 Summary and conclusions

Among the diverse family of ETGs, compact galaxies are interesting objects, typically outliers of the local mass-size relation. The compact realm spans over 5 orders of magnitude in stellar mass. Previous studies have noted that some of their properties, like the stellar populations and kinematics, appear to be related. From this, it is thought that compact galaxies may follow their own scaling relations. However, there was a gap in the mass range between cEs and CMGs, preventing to reach a more firm conclusion. In this work, we have analyzed the full MaNGA DR17 sample to find and characterize compact galaxies in this mass gap. Besides a standard mass and size cut criteria, we have used a modified surface mass density threshold to characterize the compactness of the galaxies. Our final sample consists of 37 compact galaxies out of the 10293 galaxies from the MaNGA DR17 dataset. These galaxies seem to follow the mass-size relation of $z \sim 1.5$.

Using stacked spectra up to 1 R_e, we have measured the recessional velocity and the stellar velocity dispersion of each galaxy, along with their stellar population properties, such as age, total metallicity and star formation histories. We find that our selected compact galaxies are all but one fast-rotating galaxies. We define two parameters, Δ_{50} and Δ_{90}, to characterize the formation timescales of a galaxy. We have then applied a K-Means algorithm to classify the selected compact galaxies in three different groups, as some galaxies showed clear SFH similarities. Even though the classification was constrained by the low sample number, there is a uniformity between the trends of each group. We note that two of the groups have a rather small number of galaxies. This low statistics prevents us from making solid statements and we therefore discuss each class in general terms. A detailed spatially-resolved analysis will help study each galaxy class in an individual and more detiled basis.

Then, we have compared our sample to other compact galaxies such as cEs and CMGs (which also include confirmed relic galaxies). Comparing their main stellar population and kinematic properties we can suggest different formation pathways for each class. Overall, we find that the main properties shown by each group are:

- Group A: old galaxies with early and steep SFHs. They were born 14 Gyr ago and have formed all their stars in less than 4 Gyr. They show high mean metallicities and [α/Fe] ratio (both with $\sim$ 0.3 dex). At a given mass, they show larger velocity dispersions than normal ETGs ($\sigma \sim 212$ km s^{-1}). Most of them are clear outliers of the current stellar mass-metallicity relation. In terms of their radial profiles, we see that the majority resemble the massive relic galaxies

studied to date: constant old ages, decreasing [Z/H] profiles and enhanced central [α/Fe] values, but constant at the outskirts. Therefore, we expect that some of them could be intermediate-mass relics, analogues to those at the high mass end. Moreover, some of the galaxies in this sample could be the so-called 'late-bloomers' (i.e. younger relic analogues).

- Group B: intermediate-age galaxies ($\sim$ 8 Gyr) with continuous SFH over time. Their overall metallicities are lower than those of Group A ([M/H] $\sim$ 0 dex) but similarly show a decreasing profile. The age profile for this group is an increasing one for most of its galaxies, with the centers being younger than the outskirts. They mostly have flat [α/Fe] profiles beyond $\sim 0.5\ R_e$, with an overall mean value of [α/Fe] $\sim$ 0.1 dex. Given the extended SFHs and the fact that they mostly follow the scaling relations, these galaxies are most likely the low-mass end of ETGs. Their properties make it unlikely that these galaxies have suffered any interaction with other galaxies, and are most likely formed in-situ.

- Group C: young galaxies with a mean age of $\sim$ 5 Gyr. Their SFHs reveal an early initial star formation burst, which was then halted in time and resumed only $\sim$ 4 Gyr ago. Their age profiles are mostly flat or increasing, but with young ages. We guess that these galaxies may have experienced some recent interaction that drove a cold gas flow into the galaxy center. This could have triggered the late star-forming burst. They show intermediate metallicities ([M/H] $\sim$ 0.1 dex), and the lowest mean [α/Fe] ratio ([α/Fe] $\sim$ 0 dex) among our sample. Some in fact show a slightly increasing [α/Fe] profile.

We have shown that the properties of compact galaxies shift as we consider higher masses. Both $\sigma - M_\star$ and $M_\star$-[M/H] planes show that in general, cEs are prone to be formed ex-situ. They show unusual high metallicities compared to their mass and some of them also feature high σ values. Overall, this suggests a stripping from a larger host galaxy. At the high mass end the number of CMG outliers in the $\sigma - M_\star$ and $M_\star$-[M/H] relations is lower. It is thus expected that the majority of these have an in-situ origin. The sample of compact galaxies analyzed in this study completely fills the gap between these two families. In fact, they appear to have intermediate properties, which further supports the idea that compact galaxies at different masses are all related.

Bibliography

1. S. Dodelson, F. Schmidt, in *Modern Cosmology (Second Edition)*, ed. by S. Dodelson, F. Schmidt (Academic Press, Second Edition, 2021), pp. 1–19.
2. C. J. Conselice *et al.*, *ApJ.* **830**, 83 (Oct. 2016).
3. E. P. Hubble, *ApJ.* **64**, 321–369 (Dec. 1926).
4. M. Cappellari *et al.*, *MNRAS* **379**, 418–444 (Aug. 2007).
5. M. Cappellari *et al.*, *Highlights of Astronomy* **15**, 81–81 (Nov. 2010).
6. M. Cappellari *et al.*, *MNRAS* **416**, 1680–1696 (Sept. 2011).
7. E. Toloba *et al.*, *ApJ.* **799**, 172 (Feb. 2015).
8. J. L. Sérsic, *Boletin de la Asociacion Argentina de Astronomia La Plata Argentina* **6**, 99–99 (Feb. 1963).
9. K. C. Freeman, *ApJ.* **160**, 811 (June 1970).
10. N. M. Ferrers, *Quart J. Pure and Appl. Math.* **14**, 1 (1877).
11. G. Chabrier, *PASP* **115**, 763–795 (July 2003).
12. F. Matteucci, *The chemical evolution of the Galaxy*, vol. 253.
13. A. Arcones, F.-K. Thielemann, *AAPR* **31**, 1 (Dec. 2023).
14. P. Bonifacio, *Experimental Astronomy* (June 2022).
15. B. M. Tinsley, *ApJ.* **229**, 1046–1056 (May 1979).
16. F. Matteucci, *AAP* **288**, 57–64 (Aug. 1994).
17. S. C. Trager *et al.*, *AJ* **120**, 165–188 (July 2000).
18. F. Matteucci, S. Recchi, *ApJ.* **558**, 351–358 (Sept. 2001).
19. D. Thomas *et al.*, *ApJ.* **621**, 673–694 (Mar. 2005).
20. I. G. de La Rosa *et al.*, *MNRAS* **418**, L74–L78 (Nov. 2011).
21. R. M. McDermid *et al.*, *MNRAS* **448**, 3484–3513 (Apr. 2015).
22. A. Guérou *et al.*, *ApJ.* **804**, 70 (May 2015).
23. L. Peralta de Arriba *et al.*, *MNRAS* **461**, 156–163 (Sept. 2016).

24. I. Trujillo *et al.*, *MNRAS* **382**, 109–120 (Nov. 2007).
25. F. Buitrago *et al.*, *ApJ.l* **687**, L61 (Nov. 2008).
26. E. Daddi *et al.*, *ApJ.* **626**, 680–697 (June 2005).
27. L. Peralta de Arriba, PhD thesis, University of La Laguna, Department of Astrophysics; Astrophysical Institute of the Canaries; La Palma Observatories, July 2016.
28. M. J. Drinkwater *et al.*, *PASA* **17**, 227–233 (Dec. 2000).
29. S. Phillipps *et al.*, *ApJ.* **560**, 201–206 (Oct. 2001).
30. J. P. Brodie *et al.*, *AJ* **142**, 199 (Dec. 2011).
31. S. M. Faber, *ApJ.* **179**, 423–426 (Jan. 1973).
32. P. I. Choi, P. Guhathakurta, K. V. Johnston, *AJ* **124**, 310–331 (July 2002).
33. M. J. Drinkwater *et al.*, *Nat* **423**, 519–521 (May 2003).
34. S. Shen *et al.*, *MNRAS* **343**, 978–994 (Aug. 2003).
35. A. Ferré-Mateu *et al.*, *MNRAS* **503**, 5455–5472 (June 2021).
36. R. Bezanson *et al.*, *ApJ.* **697**, 1290–1298 (June 2009).
37. T. Naab, P. H. Johansson, J. P. Ostriker, *ApJ.l* **699**, L178–L182 (July 2009).
38. L. Oser *et al.*, *ApJ.* **725**, 2312–2323 (Dec. 2010).
39. L. Oser *et al.*, *ApJ.* **744**, 63 (Jan. 2012).
40. M. Hilz, T. Naab, J. P. Ostriker, *MNRAS* **429**, 2924–2933 (Mar. 2013).
41. A. Dekel, R. Sari, D. Ceverino, *ApJ.* **703**, 785–801 (Sept. 2009).
42. A. Zolotov *et al.*, *MNRAS* **450**, 2327–2353 (July 2015).
43. R. J. Smith, *ARAA* **58**, 577–615 (Aug. 2020).
44. I. Damjanov *et al.*, *ApJ.* **793**, 39 (Sept. 2014).
45. C. Schreiber *et al.*, *AAP* **618**, A85 (Oct. 2018).
46. F. Valentino *et al.*, *ApJ.* **889**, 93 (Feb. 2020).
47. I. Martín-Navarro, G. van de Ven, A. Yıldırım, *MNRAS* **487**, 4939–4950 (Aug. 2019).
48. P. G. van Dokkum *et al.*, *ApJ.* **709**, 1018–1041 (Feb. 2010).
49. I. Trujillo *et al.*, *ApJ.l* **692**, L118–L122 (Feb. 2009).
50. B. M. Poggianti *et al.*, presented at the The Intriguing Life of Massive Galaxies, ed. by D. Thomas, A. Pasquali, I. Ferreras, vol. 295, pp. 151–154.
51. S. Wellons *et al.*, *MNRAS* **456**, 1030–1048 (Feb. 2016).
52. V. Quilis, I. Trujillo, *ApJ.l* **773**, L8 (Aug. 2013).
53. I. Trujillo *et al.*, *ApJ.l* **780**, L20 (Jan. 2014).
54. A. Ferré-Mateu *et al.*, *MNRAS* **467**, 1929–1939 (May 2017).

55. C. Spiniello *et al.*, *AAP* **646**, A28 (Feb. 2021).
56. A. van der Wel *et al.*, *ApJ.* **730**, 38 (Mar. 2011).
57. I. Trujillo *et al.*, *ApJ.* **704**, 618–628 (Oct. 2009).
58. A. Ferré-Mateu *et al.*, *MNRAS* **423**, 632–646 (June 2012).
59. B. M. Poggianti *et al.*, *ApJ.* **762**, 77 (Jan. 2013).
60. F. Buitrago *et al.*, *AAP* **619**, A137 (Nov. 2018).
61. I. Damjanov *et al.*, *ApJ.* **815**, 104 (Dec. 2015).
62. M. Stringer *et al.*, *MNRAS* **449**, 2396–2404 (May 2015).
63. M. Cebrián, I. Trujillo, *MNRAS* **444**, 682–699 (Oct. 2014).
64. C. Spiniello *et al.*, *AAP* **654**, A136 (Oct. 2021).
65. M. Cappellari, *ARAA* **54**, 597–665 (Sept. 2016).
66. K. Bekki, W. J. Couch, M. J. Drinkwater, *ApJ.l* **552**, L105–L108 (May 2001).
67. A. W. Graham, *MNRAS* **334**, 721–734 (Aug. 2002).
68. S. Paudel *et al.*, *ApJ.l* **820**, L19 (Mar. 2016).
69. J. Kormendy *et al.*, *VizieR Online Data Catalog*, J/ApJS/182/216 (Nov. 2009).
70. J. Kormendy, R. Bender, *ApJ.s* **198**, 2 (Jan. 2012).
71. M. Du *et al.*, *ApJ.* **875**, 58 (Apr. 2019).
72. A. Ferré-Mateu *et al.*, *MNRAS* **479**, 4891–4906 (Oct. 2018).
73. J. C. Forbes *et al.*, *MNRAS* **443**, 168–185 (Sept. 2014).
74. R. Pechetti *et al.*, *ApJ.* **850**, 15 (Nov. 2017).
75. A. P. Huxor *et al.*, presented at the EAS Publications Series, ed. by M. Koleva, P. Prugniel, I. Vauglin, vol. 48, pp. 257–258.
76. S. Paudel, C. H. Ree, *ApJ.l* **796**, L14 (Nov. 2014).
77. A. Ferré-Mateu, M. Mezcua, R. S. Barrows, *MNRAS* **506**, 4702–4714 (Oct. 2021).
78. M. A. Norris *et al.*, *MNRAS* **443**, 1151–1172 (Sept. 2014).
79. J. Janz *et al.*, *MNRAS* **456**, 617–632 (Feb. 2016).
80. S. Kim *et al.*, *ApJ.* **903**, 65 (Nov. 2020).
81. A. P. Huxor, S. Phillipps, J. Price, *MNRAS* **430**, 1956–1960 (Apr. 2013).
82. S. Paudel *et al.*, *MNRAS* **443**, 446–453 (Sept. 2014).
83. L. P. Bassino, J. C. Muzzio, M. Rabolli, *ApJ.* **431**, 634 (Aug. 1994).
84. K. Bekki *et al.*, *MNRAS* **344**, 1334–1344 (Oct. 2003).
85. J. Pfeffer, H. Baumgardt, *MNRAS* **433**, 1997–2005 (Aug. 2013).
86. P. Kroupa, presented at the Magellanic Clouds and Other Dwarf Galaxies, pp. 173–176.

87. R. C. Brüns *et al.*, *AAP* **529**, A138 (May 2011).

88. R. C. Brüns, P. Kroupa, *AAP* **547**, A65 (Nov. 2012).

89. K. Bundy *et al.*, *ApJ.* **798**, 7 (Jan. 2015).

90. D. G. York *et al.*, *AJ* **120**, 1579–1587 (Sept. 2000).

91. S. A. Smee *et al.*, *AJ* **146**, 32 (Aug. 2013).

92. N. Drory *et al.*, *AJ* **149**, 77 (Feb. 2015).

93. J. E. Gunn *et al.*, *AJ* **131**, 2332–2359 (Apr. 2006).

94. R. Yan, MaNGA Team, presented at the American Astronomical Society Meeting Abstracts #227, vol. 227, 312.02, p. 312.02.

95. J. .-. Fischer, H. Domínguez Sánchez, M. Bernardi, *MNRAS* **483**, 2057–2077 (Feb. 2019).

96. J. T. Mendel *et al.*, *ApJ.s* **210**, 3 (Jan. 2014).

97. H. Domínguez Sánchez *et al.*, *MNRAS* **509**, 4024–4036 (Jan. 2022).

98. J. Neumann *et al.*, *MNRAS* **513**, 5988–6012 (July 2022).

99. D. Goddard *et al.*, *MNRAS* **466**, 4731–4758 (Apr. 2017).

100. D. M. Wilkinson *et al.*, *MNRAS* **472**, 4297–4326 (Dec. 2017).

101. C. Maraston, G. Strömbäck, *MNRAS* **418**, 2785–2811 (Dec. 2011).

102. C. Maraston *et al.*, *MNRAS* **496**, 2962–2997 (Aug. 2020).

103. M. Cappellari, Y. Copin, *MNRAS* **342**, 345–354 (June 2003).

104. T. Valentinuzzi *et al.*, *ApJ.* **712**, 226–237 (Mar. 2010).

105. D. Scognamiglio *et al.*, *ApJ.* **893**, 4 (Apr. 2020).

106. G. Barro *et al.*, *ApJ.* **765**, 104 (Mar. 2013).

107. A. Charbonnier *et al.*, *MNRAS* **469**, 4523–4536 (Aug. 2017).

108. I. Damjanov *et al.*, *ApJ.* **806**, 158 (June 2015).

109. A. van der Wel *et al.*, *ApJ.* **788**, 28 (June 2014).

110. A. Yıldırım *et al.*, *MNRAS* **468**, 4216–4245 (July 2017).

111. T. Ott, *QFitsView: FITS file viewer*, Astrophysics Source Code Library, record ascl:1210.019, Oct. 2012.

112. M. Cappellari, E. Emsellem, *PASP* **116**, 138–147 (Feb. 2004).

113. M. Cappellari, *pPXF: Penalized Pixel-Fitting stellar kinematics extraction*, Astrophysics Source Code Library, record ascl:1210.002, Oct. 2012.

114. M. Sarzi *et al.*, *MNRAS* **366**, 1151–1200 (Mar. 2006).

115. P. Sánchez-Blázquez *et al.*, *MNRAS* **371**, 703–718 (Sept. 2006).

116. J. Falcón-Barroso *et al.*, *AAP* **532**, A95 (Aug. 2011).

117. I. Martín-Navarro *et al.*, *MNRAS* **451**, 1081–1089 (July 2015).

118. E. Emsellem *et al.*, *MNRAS* **379**, 401–417 (Aug. 2007).

119. A. Zoldan *et al.*, *MNRAS* **481**, 1376–1400 (Nov. 2018).

120. S. M. Sweet *et al.*, *MNRAS* **494**, 5421–5438 (June 2020).

121. A. B. Romeo, O. Agertz, F. Renaud, *MNRAS* **518**, 1002–1021 (Jan. 2023).

122. J. Falcón-Barroso *et al.*, *AAP* **632**, A59 (Dec. 2019).

123. H. Domínguez Sánchez *et al.*, *MNRAS* **489**, 5612–5632 (Nov. 2019).

124. A. Bittner *et al.*, *AAP* **628**, A117 (Aug. 2019).

125. D. Langeroodi *et al.*, *arXiv e-prints*, arXiv:2212.02491 (Dec. 2022).

126. A. Gallazzi *et al.*, *MNRAS* **370**, 1106–1124 (Aug. 2006).

127. C. A. Tremonti *et al.*, *ApJ.* **613**, 898–913 (Oct. 2004).

128. I. Saviane *et al.*, *Mem.SAI* **85**, 417 (Jan. 2014).

129. A. Henry *et al.*, *ApJ.* **919**, 143 (Oct. 2021).

130. B. Panter *et al.*, *MNRAS* **391**, 1117–1126 (Dec. 2008).

131. E. N. Kirby *et al.*, *AJ* **159**, 46 (Feb. 2020).

132. A. Ferré-Mateu *et al.*, *ApJ.* **808**, 79 (July 2015).

133. A. R. Gallazzi *et al.*, *MNRAS* **502**, 4457–4478 (Apr. 2021).

134. J. B. Hyde, M. Bernardi, *MNRAS* **394**, 1978–1990 (Apr. 2009).

135. M. Bernardi *et al.*, *MNRAS* **412**, L6–L10 (Mar. 2011).

136. M. Cappellari *et al.*, *MNRAS* **432**, 1862–1893 (July 2013).

137. M. Sereno, S. Ettori, *MNRAS* **450**, 3675–3695 (July 2015).

138. A. E. Evrard *et al.*, *ApJ.* **672**, 122–137 (Jan. 2008).

139. J. B. Hyde, M. Bernardi, *MNRAS* **396**, 1171–1185 (June 2009).

140. H. J. Zahid *et al.*, *ApJ.* **832**, 203 (Dec. 2016).

141. E. Emsellem *et al.*, *MNRAS* **414**, 888–912 (June 2011).

142. M. Bílek, P.-A. Duc, E. Sola, *arXiv e-prints*, arXiv:2210.02478 (Oct. 2022).

143. A.-M. Weijmans *et al.*, *MNRAS* **444**, 3340–3356 (Nov. 2014).

144. C. Foster *et al.*, *MNRAS* **472**, 966–978 (Nov. 2017).

145. T. Naab *et al.*, *MNRAS* **444**, 3357–3387 (Nov. 2014).

146. E. Emsellem *et al.*, *MNRAS* **352**, 721–743 (Aug. 2004).

147. R. Flores-Freitas *et al.*, *MNRAS* **512**, 245–264 (May 2022).

148. P. Sánchez-Blázquez *et al.*, *MNRAS* **377**, 759–786 (May 2007).